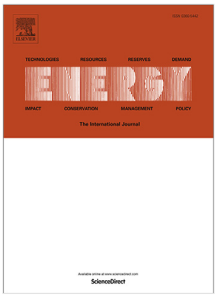
Journal Pre-proof



Coupled hydro-aero-turbo dynamics of liquid-tank system for wave energy harvesting: Numerical modellings and scaled prototype tests

Chongwei Zhang, Xunhao Zhu, Cheng Zhang, Luofeng Huang, Dezhi Ning

PII: S0360-5442(25)02332-1
DOI: https://doi.org/10.1016/j.energy.2025.136690
Reference: EGY 136690

To appear in: *Energy*

Received date : 8 March 2025
Revised date : 30 April 2025
Accepted date : 19 May 2025

Please cite this article as: C. Zhang, X. Zhu, C. Zhang et al., Coupled hydro-aero-turbo dynamics of liquid-tank system for wave energy harvesting: Numerical modellings and scaled prototype tests. *Energy* (2025), doi: https://doi.org/10.1016/j.energy.2025.136690.

This is a PDF file of an article that has undergone enhancements after acceptance, such as the addition of a cover page and metadata, and formatting for readability, but it is not yet the definitive version of record. This version will undergo additional copyediting, typesetting and review before it is published in its final form, but we are providing this version to give early visibility of the article. Please note that, during the production process, errors may be discovered which could affect the content, and all legal disclaimers that apply to the journal pertain.

© 2025 Published by Elsevier Ltd.

Journal Pre-proof

Essential title page information

Title: Coupled hydro-aero-turbo dynamics of liquid-tank system for wave energy harvesting: Numerical modellings and scaled prototype tests

Author names and affiliations:
Chongwei Zhang[a], Xunhao Zhu[b], Cheng Zhang[c], Luofeng Huang[d], Dezhi Ning[e]
(N.B. The family name is underlined.)

[a] State Key Laboratory of Coastal and Offshore Engineering, Dalian University of Technology, No. 2 Linggong Road, Dalian, 116024, P.R. China.
chongweizhang@dlut.edu.cn
[b] State Key Laboratory of Coastal and Offshore Engineering, Dalian University of Technology, No. 2 Linggong Road, Dalian, 116024, P.R. China.
zxunhao@163.com
[c] State Key Laboratory of Coastal and Offshore Engineering, Dalian University of Technology, No. 2 Linggong Road, Dalian, 116024, P.R. China.
2547833784@mail.dlut.edu.cn
[d] Faculty of Engineering and Applied Sciences, Cranfield University, Cranfield MK43 0AL, United Kingdom
luofeng.huang@cranfield.ac.uk
[e] State Key Laboratory of Coastal and Offshore Engineering, Dalian University of Technology, No. 2 Linggong Road, Dalian, 116024, P.R. China. dzning@dlut.edu.cn

Corresponding author:
Chongwei Zhang
State Key Laboratory of Coastal and Offshore Engineering, Dalian University of Technology, Dalian 116024, China
Tel +86-(0)411-84708520-8403
Email: chongweizhang@dlut.edu.cn

Journal Pre-proof

Energy, Volume 330, September 2025, Article number 136690
DOI: 10.1016/j.energy.2025.136690

Revised Manuscript (without track changes)
Click here to view linked References

Coupled hydro-aero-turbo dynamics of liquid-tank system for wave energy harvesting: Numerical modellings and scaled prototype tests

Chongwei Zhang[a,b,*,1], Xunhao Zhu[a], Cheng Zhang[a], Luofeng Huang[c] and Dezhi Ning[a,**]

[a]State Key Laboratory of Coastal and Offshore Engineering, Dalian University of Technology, Dalian, 116024, P.R. China
[b]Shanghai Engineering Research Center of Offshore Wind Energy Development and Utilization, Shanghai Investigation, Design & Research Institute Co., Ltd, Shanghai, 200335, P.R. China
[c]School of Water, Energy and Environment, Cranfield University, Cranfield, MK43 0AL, United Kingdom

ARTICLE INFO

Keywords:
wave energy
liquid sloshing
wave energy converter
power take-off

ABSTRACT

The wave-energy-harvesting (WEH) liquid tank with an air-turbine system has distinct advantages in survivability and durability. Its air-turbine effects have long been simplified using orifices, perforated plates, or empirical formulae. This study proposes an integrated numerical model to couple with actual turbine motions. A series of experiments are conducted on a scaled prototype of the WEH liquid tank with an impulse air turbine system. Benchmark experimental data are obtained for validation of the numerical model. The proposed integrated numerical model accurately reproduces the experimental observations. The effects of turbine parameters on the coupled hydro-aero-turbo behavior are systematically investigated. The optimal power take-off damping for the WEH liquid tank is identified. A multi-layered impulse air turbine system (MLATS) is creatively introduced into the liquid-tank system to explore its capability in improving efficiency and reliability. Compared to the single-rotor case, the MLATS with three rotors can increase the average power output of the WEH liquid tank by up to 40%. Through a series of failure tests, a three-rotor turbine shows greater reliability than a conventional single-rotor turbine.

1. Introduction

Ocean wave energy has received extraordinary attention in recent years due to its great potential to reduce carbon footprint [1]. A large variety of wave energy converter (WEC) concepts have been proposed to convert wave power into electricity. To date, three dominant technical streams of WECs can be identified according to the power take-off (PTO) principle, *i.e.* the pneumatic [2], the oscillating-buoy (OB) [3], and the overtopping (OT) types [4–6]. The pneumatic type WECs include the oscillation water column (OWC)[7–9], the backward bent duct buoy (BBDB)[10–12], and so on; and the OB type WECs can be further classified as point absorbers [13–15], buoyancy pendulums [16, 17], and gravitational pendulums [18]. Over the past decades, people have made massive efforts to improve the energy conversion efficiency of specific WEC concepts in the laboratory [19].

From the laboratory to the real sea, survivability is another important criterion for the success of a practical WEC product [20]. A practical WEC product, often with a designed lifetime of at least twenty years, must withstand extreme wave conditions with a return period of 100 years [21]. Especially in large storm waves or rogue waves, the wave height may reach 20 m [22, 23]. Such extreme waves can generate destructive slamming loads on the device, threatening the survivability of a WEC device [24, 25]. Unfortunately, for conventional WECs, a common inherent weakness in the design is that the moving parts, which are often the core power take-off (PTO) components of the device, are constantly exposed to the marine environment[26]. Extreme wave loads and various types of corrosions that are often overlooked in the design phase have been identified as the main cause of most technical failures of WECs in real ocean conditions [20]. Exposing the most essential but weakest working units to harsh marine environment is a significant threat to the survivability of a WEC device[27].

To improve the survivability of WECs in real sea, some researchers turn to an alternative direction of concept design, i.e. the "enclosed WEC" (En-WEC for short). The key idea is to shelter all mechanical and electrical components inside a closed hull, so that all moving parts are isolated from the aggressive sea environment. For ease

*E-mail: chongweizhang@dlut.edu.cn
**E-mail: dzning@dlut.edu.cn
ORCID(s): 0000-0002-0062-4548 (C. Zhang)

Published by Elsevier. This is the Author Accepted Manuscript issued with: Creative Commons Attribution License (CC:BY 4.0).
The final published version (version of record) is available online at DOI:10.1016/j.energy.2025.136690. Please refer to any applicable publisher terms of use.

Journal Pre-proof

of distinction, the conventional pneumatic, OB-, or OT-type WECs are referred to by the term “exposed WEC” (Ex-WEC for short). En-WECs can be further categorised as the “dry-tank” and “liquid-tank” type, based on whether the internal PTO system is directly driven by the hull or indirectly driven via oscillating liquids inside the hull. A detailed classification of working principles of WECs is summarised in Fig. 1.

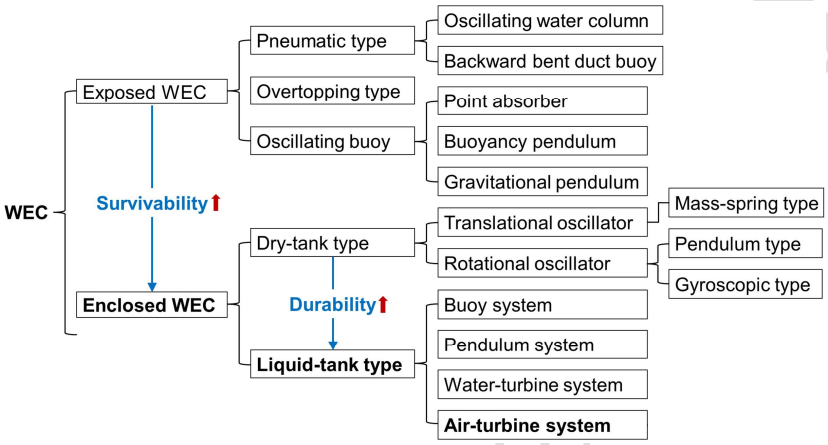


Figure 1: Classification of working principles of wave energy converters

For dry-tank En-WECs, the mathematical models of their PTO systems can be identified as translational or rotational oscillators, as illustrated in Fig. 2. The most typical translational oscillator is the mass-spring (MS) system in either the horizontal or vertical direction [28–31]. The rotational oscillators are often pendulum or gyroscopic systems [20, 32–35]. Compared with conventional Ex-WECs, dry-tank En-WECs naturally have better survivability. However, they still face some inherent challenges. For example, a large stroke for the MS system or a large length of pendulum is required inside the limited hull.

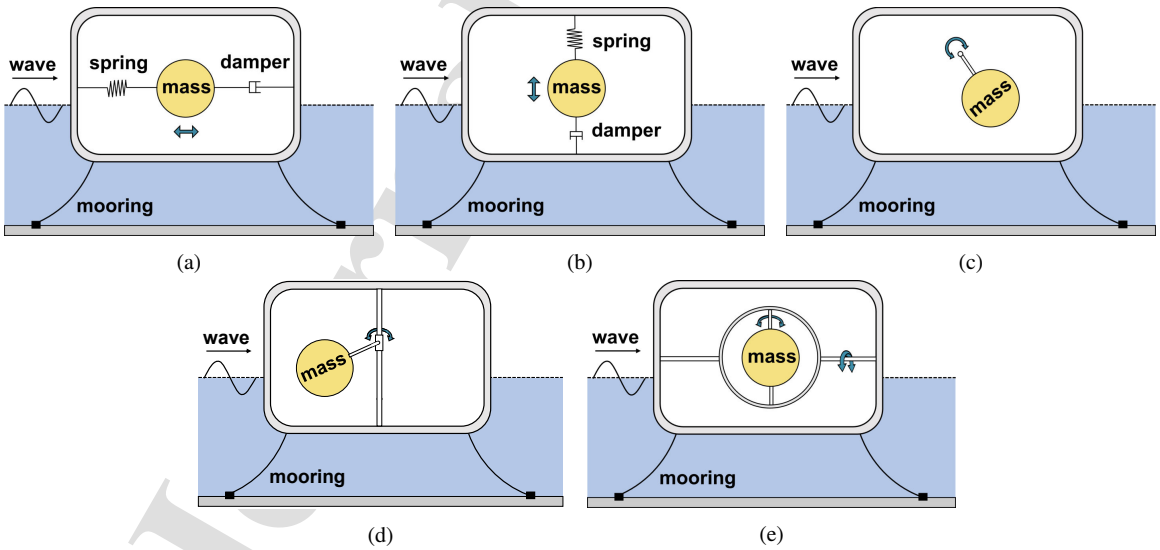


Figure 2: Mechanical principle of dry-tank En-WEC with (a) horizontal mass-spring system; (b) vertical mass-spring system; (c) horizontal-axis pendulum system; (d) vertical-axis pendulum system; and (e) gyroscopic system

Journal Pre-proof

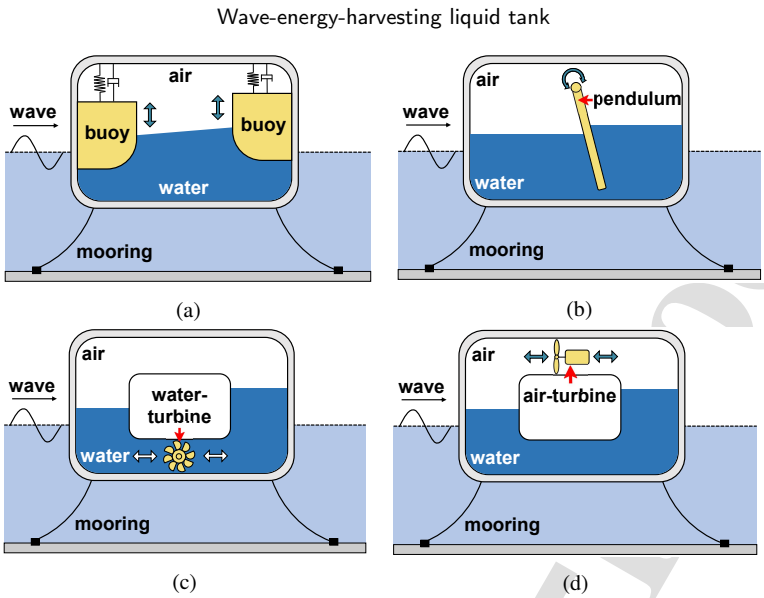


Figure 3: Mechanical principle of liquid-tank En-WEC with (a) buoy system [36]; (b) pendulum system; (c) water-turbine system; and (d) air-turbine system

To further improve the durability of an En-WEC, a useful strategy is to introduce sloshing liquid (as an extra buffering medium) between the floating hull and the internal PTO system. The internal liquid can first absorb the kinetic energy of the hull for temporary storage and then drive the PTO system. The inherent challenges of the dry-tank En-WEC are naturally addressed by the liquid-tank En-WEC. Natural frequencies of the system can be controlled easily by adjusting the filling level of the liquid tank within a limited internal space.

Four categories of liquid-tank En-WECs can been recognised in literature, as shown in Fig. 3. The first category was first established by Zhang et al. [36], which utilises the buoy-type PTO system to harvest sloshing wave energy in the floating liquid tank, as shown in Fig. 3(a). In the second category (Fig. 3(b)), a pendulum instead of buoys was used as the PTO system in liquid tank [37]. In the third category (Fig. 3(c)), the liquid tank is U-shaped with a cross-flow water-turbine install in the horizontal tube, converting kinetic energy of bidirectional flows into electricity [38, 39]. In the fourth category (Fig. 3(d)), a pipe is used to connect two air chambers of the U-shaped liquid tank, in which an air-turbine system is used to harvest the energy of bidirectional air flows [40]. A typical liquid-tank En-WEC of the fourth category is the "UGEN" WEC, an asymmetric floater with an interior U-shaped liquid tank [41].

In previous theoretical or numerical studies of pneumatic type liquid-tank En-WECs, a common practice was to simulate the turbine effect using an orifice, a perforated plate, or an empirical formula [40–43]. However, without a real turbine simulation, no one actually knows whether most of the captured wave energy is lost as heat or is successfully converted into electricity through the turbine system. To bridge this gap, this study aims to develop an integrated numerical model for pneumatic liquid-tank En-WECs. Simulations of real turbine motions should be included in the numerical model. The transient dynamic effects and energy harvesting of the air-turbine system in liquid-tank En-WECs can be evaluated explicitly. In addition, to validate the integrated numerical model, a scaled prototype of the wave-energy-harvesting (WEH) liquid tank with an impulse air turbine system is created. A series of physical experiments are conducted on the prototype, to examine the dynamic behavior of a liquid tank with a physical air-turbine system. The geometry parameters of the liquid tank and air turbine were specifically simplified to ensure the model could be reproduced easily. The experiments also fill an important gap in the benchmark experimental database for liquid-tank En-WECs. After validating the numerical method for conventional air turbines, this study will test a creative strategy that integrates the multi-layered impulse air turbine system (MLATS) into the liquid tank. Effects of the MLATS on enhancing the efficiency and reliability of the liquid-tank En-WEC will be investigated.

Journal Pre-proof

2. Concept description of wave-energy-harvesting liquid tank

This study considers a liquid-tank En-WEC, as shown in Fig. 4. Multiple U-shaped WEH liquid tanks are arranged in parallel inside the buoy. The air duct is equipped with a novel MLATS that converts the kinetic energy of air flow into electricity. During operation, the buoy excites internal liquid-body oscillations, which further causes bi-directional air flows through the air duct. The airflows can continuously drive the MLATS to produce electricity.

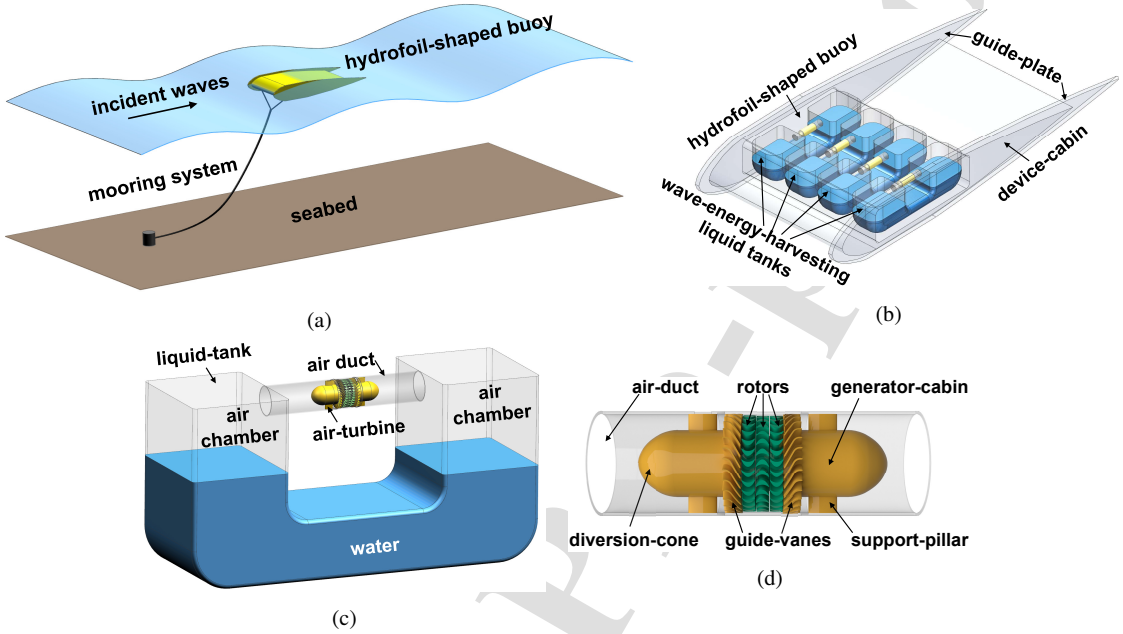


Figure 4: (a) External appearance of hydrofoil-shaped buoy; (b) concept of wave-energy-harvesting liquid tanks inside the buoy; (c) components of wave-energy-harvesting liquid tank; (d) components of multi-layered impulse air-turbine system

The details of the MLATS are illustrated in Fig. 4 (d). Multiple layers of rotors are installed between two sets of guide-vanes. Each rotor is connected to an isolated generator inside the generator cabin. Adjacent rotors are installed in the opposite way. As a result, the deflected airflow behind one rotor hits the blades of the downstream rotor, giving a tangential drive to the rotor. Because of the symmetrical nature of the guide vanes and rotor blade, each rotor always rotates in the same direction, regardless of the airflow direction.

This study specifically designed three MLATSs, namely Turbine-L1, Turbine-L2, and Turbine-L3, as shown in Fig. 5. Turbine-L1, Turbine-L2, and Turbine-L3 are featured with one, two, and three layers of rotors, respectively. The following parameters are introduced to define the geometry of the turbine system. The external diameter of guide vanes (also the internal diameter of the air duct) is denoted by d_a. The diameter of the cylindrical main body is d_c. The total length of the turbine system (the distance between two vertices of diversion cones) is l_t. The breadth of each rotor is b_r. The gap size between adjacent rotors is l_b. The spacing between guide vanes and the adjacent rotor is l_r. For each rotor blade, the height measured from the blade root on the cylinder to the blade tip is h_r; the cross-sectional profile is formed by an circular arc of radius r_p and an elliptical arc with semi-major axis I_a and semi-minor axis I_b; and the angle of attack is θ_1. For each guide vane, its has a thickness b_g and a height $h_g = (d_a - d_c)/2$; the cross-sectional profile is formed by a straight segment of length l_c, and an arc of radius r_g and curvature angle θ_2; both tips are rounded off by ellipses of a semi-major axis I_c and a semi-minor axis I_d. The angle of incidence of each guide vane is θ_3, and the distance between guide vanes is l_g. The chord length of the rotor blade is l_p.

3. Scaled prototype and experimental set-ups

One focus of this study is to create a physical benchmark database for liquid-tank En-WECs. To ensure the model is easily reproducible, this study deliberately simplifies the shape and internal structures. The motion of the tank is also

Journal Pre-proof

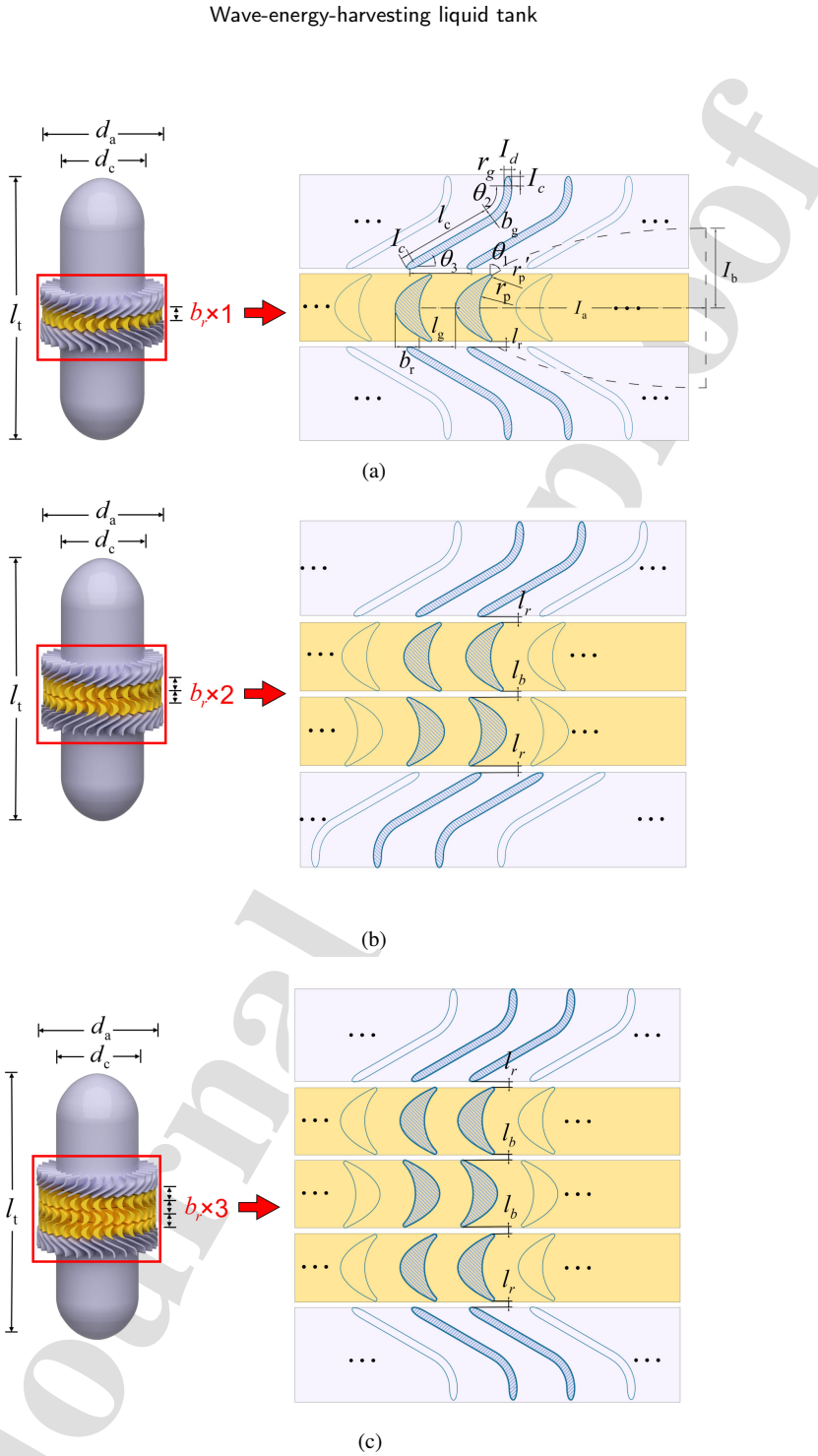


Figure 5: Design parameters of multi-layered impulse air turbine systems for (a) Turbine-L1, (b) Turbine-L2, and (c) Turbine-L3

Journal Pre-proof

Table 1
Geometry parameters of liquid tank model in physical experiment

Parameter	Value	Unit	Parameter	Value	Unit
L	0.600	m	b	0.150	m
B	0.300	m	h	0.150	m
H_t	0.600	m	d_a	0.069	m
H	0.250	m	d_w	1.0	mm

explicitly defined. With this simplification, any researcher can easily set the parameters to validate their theoretical or numerical model for liquid-tank En-WECs.

The simplified liquid tank is shown in Fig. 6. The liquid tank has a rectangular cross section. The inner space of the liquid tank has a height of H_t and a breadth of B. The length and height of the horizontal water column in the tank are L and h, respectively. For each vertical water column, the height is H and the breadth is b. The WEH liquid tank model is fixed on a shaking table. The shaking table has a working area of 1m × 1m. It can support a model weighing up to 50kg. Therefore, the length of the tank is set to $L = 0.600$ m, the width of the tank is $B = 0.300$ m, and the liquid depth in the tank is set to $H = 0.25$ m. These dimensions are within the shaking table's maximum loading capacity. The liquid tank is specially designed as a simple combination of rectangular plates. The liquid tank consists of polymethyl methacrylate plates and tubes with a thickness of $d_w = 1.0$ mm. More detailed geometry parameters of the liquid tank model are listed in Table 1.

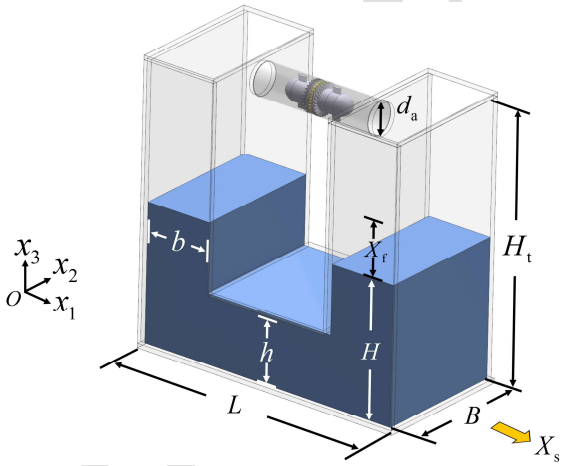


Figure 6: Illustration of wave-energy-harvesting liquid tank model

A circular air duct with a diameter of d_a links the tops of two sealed chambers of the liquid tank. The Turbine-L1 model is installed in the air duct. All components of Turbine-L1 are made of laser-cured resin materials through 3D printing technology. The cylindrical main body of the turbine system has two sets of 30 guide vanes. Each rotor has 30 identical blades. The detailed geometry parameters of the air-turbine model are described in Table 2. The performance of impulse turbines is sensitive to the rotor blade tip clearance l_s, particularly when l_s ranges from 0.25% to 4% of the axial chord length of the rotor blades. However, once l_s exceeds 4%, its influence on turbine performance becomes limited. Due to experimental constraints, the rotor tip clearance in this study is set to 0.5 mm, corresponding to 6% of the axial chord length of the rotor blades simulations [44, 45]. In the axial direction, the flow domain upstream and downstream of the turbine guide vanes is limited to four blade chord lengths to ensure sufficiently developed turbulence at the upstream of the guide vanes. The axial length of the aero–turbo region is determined by the combined width of a single rotor and the gap between the guide vanes and the adjacent rotor, as defined in the prototype configuration. A servo motor connects to the rotor, acting as the source of the turbine's inherent resistance and measures the rotor's

Journal Pre-proof

Table 2
Geometry parameters of air-turbine model in physical experiment

Parameter	Value	Unit	Parameter	Value	Unit
θ_1	60	°	l_c	1.5	mm
θ_2	60	°	l_d	1.0	mm
θ_3	30	°	l_b	1.1	mm
b_g	1.0	mm	l_c	10.8	mm
b_n	3.1	mm	l_g	7.8	mm
b_r	8.5	mm	l_p	8.5	mm
d_a	69.0	mm	l_r	1.1	mm
d_c	47.0	mm	l_s	0.5	mm
h_g	6.0	mm	l_t	166.5	mm
h_r	10.0	mm	r_g	4.8	mm
I_a	48.0	mm	r_p	5.8	mm
I_b	10.3	mm	r'_p	0.2	mm

rotational speed. Two ultrasonic wave gauges are installed at the centres of the ceilings of two sealed chambers to monitor the elevation histories of the free surface in the liquid tank.

The scaled prototype of the WEH liquid tank with Turbine-L1 is shown in Fig. 7. Harmonic excitations in the horizontal direction are generated to simulate the surge motion of the floater. The excitation parameters are carefully calculated. This ensures that the excitation frequency range covers the natural sloshing frequency of the liquid column. The excitation amplitude is $A = 0.022$ m, which is selected to satisfy the small-amplitude assumption and ensure safe operation within the shaking table's capacity.

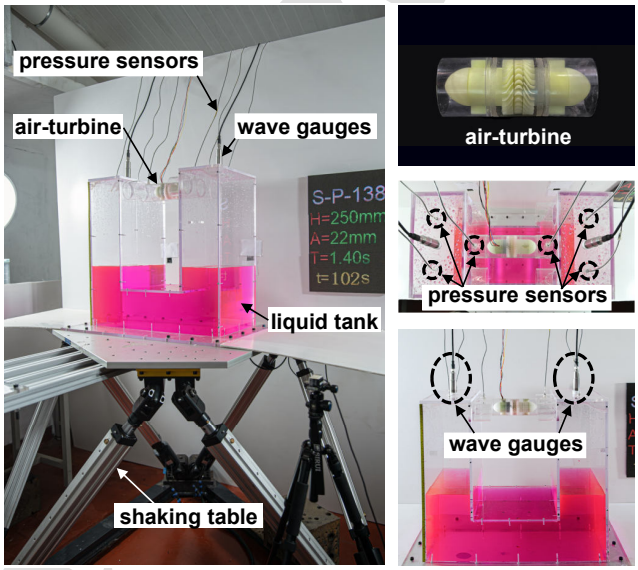


Figure 7: Scaled prototype of wave-energy-harvesting liquid tank and measurement system

4. Theoretical model for wave-energy-harvesting liquid tank

This section describes the theoretical model for wave-energy-harvesting liquid tank. The mathematical foundation is borrowed from that used in OWC simulations. The following assumptions are made: (1) The sealed liquid tank is treated as an adiabatic system with compressible internal gas. (2) The free surface disturbances are assumed to be small relative to the tank dimensions, and there is no surface breaking. (3) Instead of a linear relationship associated with

Journal Pre-proof

laminar flow, a nonlinear characteristic is adopted to more accurately capture the throttling behavior of the impulse turbine.

The Lagrangian equation of the liquid-tank system in this study is as follows:

$$\frac{\mathrm{d}}{\mathrm{d}t}\left(\frac{\partial E_1}{\partial \dot{q}_\alpha}\right) - \frac{\partial E_1}{\partial q_\alpha} + \frac{\partial E_2}{\partial q_\alpha} = F_{\mathrm{Q}} \tag{1}$$

where E_1 is the kinetic energy, E_2 is the potential energy, q_α is the generalized coordinate,$\dot{q}_{\mathrm{a}} = dq_{\mathrm{a}}/dt$, and F_{Q} is the non-conservative force, including the non-conservative force exerted by the gas pressure on the liquid column and the non-conservative damping force exerted by the tank on the liquid.

Given that the density of air is significantly lower than that of water, the kinetic and potential energy contributions from the gas phase are considered negligible. Accordingly, the kinetic energy of the liquid within the sealed system can be expressed as follows:

$$E_{\mathrm{l}} = \rho A_{\mathrm{h}}(H - X_{\mathrm{f}})(\dot{X}_{\mathrm{f}}^2 + \dot{X}_{\mathrm{s}}^2) + \frac{1}{2}\rho A_{\mathrm{v}} d(\dot{X}_{\mathrm{f}}^2 - \dot{X}_{\mathrm{s}}^2)^2 \tag{2}$$

where ρ is the density of the liquid, A_{v} is the cross-sectional area of the horizontal segment of the liquid column, A_{h} is the cross-sectional area of the vertical segment of the liquid column, d is the length of the horizontal segment of the liquid column, X_{f} denotes the vertical displacement of the right-side liquid column, with $\dot{X}_{\mathrm{f}} = dX_{\mathrm{f}}/dt$, X_{s} denotes the horizontal displacement of the tank, with $\dot{X}_{\mathrm{s}} = dX_{\mathrm{s}}/dt$, and H is the initial liquid depth.

$$E_2 = \frac{1}{2}\rho g A_{\mathrm{h}}(H - X_{\mathrm{f}})^2 + \frac{1}{2}\rho g A_{\mathrm{h}}(H + X_{\mathrm{f}})^2 \tag{3}$$

where g is the gravitational acceleration.

The non-conservative force F_{Q} consists of two components: the elastic force exerted by the gas on the liquid column, denoted as F_{k}, and the turbulent dissipation force within the liquid, denoted as F_{q}. The elastic force F_{k} is proportional to the square of the liquid velocity, while λ is the dimensionless coefficient representing the intensity of turbulent dissipation. It is important to note that the non-conservative forces acting on the two liquid columns are in opposite directions. Additionally, F_{q} always acts in the direction opposite to the motion of the liquid column.

$$F_{\mathrm{Q}} = F_{\mathrm{k}} + F_{\mathrm{q}} \tag{4}$$

$$F_{\mathrm{k}} = -p_{\mathrm{r}} A_{\mathrm{h}} + p_{\mathrm{l}} A_{\mathrm{h}} \tag{5}$$

$$F_{\mathrm{q}} = -\frac{1}{2}\rho\lambda A_{\mathrm{v}} \left|\dot{X}_{\mathrm{f}}\right| \dot{X}_{\mathrm{f}} \tag{6}$$

where p_{l} and p_{r} represent the time-varying air pressures in the left and right chambers, respectively.

By substituting Eq. (2) through Eq. (6) into equation Eq. (1), the liquid column dynamics model of the system is obtained as shown in Eq. (7):

$$(\rho d A_{\mathrm{v}} + 2\rho A_{\mathrm{h}} h_{\mathrm{v}})\ddot{X}_{\mathrm{f}} + \frac{1}{2}\rho A_{\mathrm{v}}\lambda \left|\dot{X}_{\mathrm{f}}\right| \dot{X}_{\mathrm{f}} + 2\rho g A_{\mathrm{h}} \dot{X}_{\mathrm{f}} + P_0 P A_{\mathrm{h}} = \rho d A_{\mathrm{v}} \ddot{X}_{\mathrm{s}} \tag{7}$$

$$P = \frac{p_{\mathrm{r}} - p_{\mathrm{l}}}{p_{\mathrm{e}}} \tag{8}$$

where P_0 is the initial dimensionless pressure difference, P is the dimensionless pressure difference between the two chambers, and P_{e} is the average gas pressure in both chambers.

The turbine modeling approach is consistent with the one proposed by Fonseca et al. [42]. The “air spring” effect is considered during the gas exchange process in the chambers. The gas is assumed to behave as an ideal gas undergoing

Journal Pre-proof

adiabatic and isentropic flow. During the gas exchange process, the pressure and temperature distributions in each chamber are assumed to be uniform. The thermodynamic process of the gas within each chamber can be determined by the first law of thermodynamics:

$$Q = \Delta U + W \tag{9}$$

$$\Delta U = \frac{aM_{\mathrm{g}}}{2M_{\mathrm{mol}}} R\Delta T_{\mathrm{g}} \tag{10}$$

$$W = \int p\mathrm{d}V \tag{11}$$

where Q is the heat absorbed by the gas, U is the internal energy of the gas, W is the work done by the gas in each chamber on other parts of the liquid tank, M_{g} is the mass of the gas, M_{mol} is the molar mass of the gas, a is the degree of freedom of air molecules, typically taken as 5, R is the universal gas constant, T_{g} is the temperature of the gas, p is the gas pressure, and V is the gas volume. Substituting Eq. (10) and Eq. (11) into equation Eq. (9) yields the differential form of the equation:

$$\mathrm{d}Q = \frac{\gamma p\mathrm{d}V + V\mathrm{d}p}{\gamma - 1} \tag{12}$$

where γ is the specific heat ratio.

Since the system is assumed to be adiabatic, the heat absorbed by the gas in each chamber (denoted as Q) occurs only during the gas exchange process between the chambers. This heat transfer has two components. One is the direct heat transfer Q_1 carried by the exchanged gas. The other is the convective heat transfer Q_2 that results from thermal mixing within the chamber during exchange. These components are calculated by:

$$Q_1 = c_p \left(\sum G_{\mathrm{in}} T_{\mathrm{in,stagn}} - \sum G_{\mathrm{out}} T_{\mathrm{out,stagn}} \right) \tag{13}$$

$$Q_2 = k_{\mathrm{h}} S_{\mathrm{h}} (T_{\mathrm{ex}} - T_{\mathrm{in}}) \tag{14}$$

Here, c_{p} is the specific heat at constant pressure. G_{in} and G_{out} are the mass flow rates of gas inhaled into and exhaled from each chamber, respectively. $T_{\mathrm{in,stagn}}$ and $T_{\mathrm{out,stagn}}$ are the adiabatic stagnation temperatures of the gas inhaled into and exhaled from the chamber, respectively. k_{h} is the heat transfer coefficient. S_{h} is the heat transfer surface area. T_{ex} and T_{in} are the gas temperatures outside and inside the chamber, respectively.

$$\frac{Rk_{\mathrm{h}}S_{\mathrm{h}}}{c_p pV} \left(T_{\mathrm{ex}} - T_{\mathrm{in}}\right) + \frac{1}{M_{\mathrm{g}}T_{\mathrm{g}}} \left(\sum G_{\mathrm{in}} T_{\mathrm{in,stagn}} - \sum G_{\mathrm{out}} T_{\mathrm{out,stagn}} \right) = \frac{\mathrm{d}p}{\gamma p} + \frac{\mathrm{d}V}{V} \tag{15}$$

Under the assumption of small-amplitude excitation, the time-varying state variables during the gas exchange process—such as p,V,T_{g},and M_{g}—can be expressed as the sum of the average state variables of the two chambers (p_{e}, V_{e}, T_{e}, M_{e}) and small perturbation terms (dp,dV,dT,dM). For the sake of simplifying the governing equations, it is acceptable to further approximate these variables by their average values alone, leading to the following equation:

$$\frac{Rk_{\mathrm{h}}S_{\mathrm{h}}}{c_p p_{\mathrm{e}} V_{\mathrm{e}}} \left(T_{\mathrm{ex}} - T_{\mathrm{in}}\right) + \frac{1}{M_{\mathrm{e}}T_{\mathrm{e}}} \left(\sum G_{\mathrm{in}} T_{\mathrm{in,stagn}} - \sum G_{\mathrm{out}} T_{\mathrm{out,stagn}} \right) = \frac{\mathrm{d}p}{\gamma p_{\mathrm{e}}} + \frac{\mathrm{d}V}{V_{\mathrm{e}}} \tag{16}$$

Since the excitation is of small amplitude, the difference between $T_{\mathrm{in,stagn}}$, $T_{\mathrm{out,stagn}}$, and T_{e} in each chamber can be neglected. Eq. (16) simplifies to the following form:

$$\frac{Rk_{\mathrm{h}}S_{\mathrm{h}}}{c_p p_{\mathrm{e}} V_{\mathrm{e}}} \left(T_{\mathrm{ex}} - T_{\mathrm{in}}\right) + \frac{1}{M_{\mathrm{e}}} \left(\sum G_{\mathrm{in}} - \sum G_{\mathrm{out}} \right) = \frac{\mathrm{d}p}{\gamma p_{\mathrm{e}}} + \frac{\mathrm{d}V}{V_{\mathrm{e}}} \tag{17}$$

Journal Pre-proof

During the gas exchange process, the volume of gas expelled from the right chamber is equal to the volume of gas inhaled into the left chamber, Eq. (17) can be simplified as follows:

$$\frac{\mathrm{d}p_\mathrm{r} - \mathrm{d}p_\mathrm{l}}{\gamma p_\mathrm{e}} = -\frac{\mathrm{d}V_\mathrm{r} - \mathrm{d}V_\mathrm{l}}{V_\mathrm{e}} - \frac{2Rk_\mathrm{h}S_\mathrm{h}}{c_\mathrm{p}p_\mathrm{e}V_\mathrm{e}}\left(T_\mathrm{r} - T_\mathrm{r}\right) - \frac{2\sum G_{\mathrm{out(r)}}}{M_\mathrm{e}} \tag{18}$$

The relationship between the chamber volume and liquid surface displacement is given by

$$\mathrm{d}V_\mathrm{r} - \mathrm{d}V_\mathrm{l} = -2A_\mathrm{v}\mathrm{d}X_\mathrm{f} \tag{19}$$

Since the volume of the sealed liquid tank is small and gas exchange occurs frequently, it can be assumed that the gas temperature in the left and right chambers is the same, i.e., $T_\mathrm{r} = T_\mathrm{l}$. Based on these assumptions, Eq. (18) can be further simplified to Eq. (20).

$$\mathrm{d}(\frac{p_\mathrm{r} - p_\mathrm{l}}{p_\mathrm{e}}) = 2\gamma\frac{A_\mathrm{v}}{V_\mathrm{e}}\mathrm{d}X_\mathrm{f} - 2\gamma\frac{\sum G_{\mathrm{out(r)}}}{M_\mathrm{e}} \tag{20}$$

Assuming turbulence is managed through an impulsed turbine, it can be considered that $G_{\mathrm{out(r)}}$ is proportional to the square root of P, with a dimensionless turbulence coefficient c_t introduced. The thermodynamic model of the gas within the sealed liquid tank can thus be expressed as:

$$\dot{P} = \frac{\psi}{l_\mathrm{a}}\dot{X}_\mathrm{f} - c_\mathrm{t}\omega_\mathrm{l}\sqrt{|P|}\mathrm{sgn}(P) \tag{21}$$

where l_a is the effective length of the gas, $l_\mathrm{a} = V_\mathrm{e}/A_\mathrm{v}$. ψ is the dimensionless gas parameter with $\psi = 2\gamma$, c_t is the dimensionless turbulence coefficient, and ω_l is the liquid's natural frequency. Eq.(7) and Eq.(21) together form the mathematical model for the WEH liquid tank.

5. Integrated numerical model for wave-energy-harvesting liquid tank

5.1. Governing equations and Boundary conditions

A Cartesian coordinate system $O-x_1x_2x_3$ is established, with its origin O coinciding with the center of the bottom of the liquid tank. The Ox_1-axis is along the lengthwise edge of the tank, the Ox_3-axis points upward, and the Ox_2-axis is determined by the right-hand rule.

The fluid domain consists of both the liquid and air phases. The air phase is considered compressible to assess the turbine's energy conversion performance. The viscous flow theory is used to describe the motion of fluid flows. Hereafter, all equations are expressed in tensor notation, following the Einstein summation convention. The Reynolds-Averaged Navier-Stokes (RANS) equations are adopted as the governing equations for the fluid domain:

$$\begin{aligned}
&\frac{\partial\rho}{\partial t} + \frac{\partial(\rho\overline{u}_i)}{\partial x_i} = 0\\
&\frac{\partial(\rho\overline{u}_j)}{\partial t} + \frac{\partial(\rho\overline{u}_i\overline{u}_j)}{\partial x_i} = f_i - \frac{\partial\overline{p}}{\partial x_j} + \frac{\partial\tau_{ij}}{\partial x_i}
\end{aligned} \tag{22}$$

where ρ is the density of the fluid, $\overline{u}_i$ ($i = 1, 2, 3$ corresponding to the spatial directions) is the mean velocity component in the i-th direction, and f_i is the body force, $\overline{p}$ is the mean pressure and τ_{ij} is the stress tensor. All fluid–structure interfaces are subjected to non-slip wall boundary conditions. For a Newtonian fluid, the stress tensor can be written as:

$$\tau_{ij} = \kappa\left(\frac{\partial\overline{u}_i}{\partial x_j} + \frac{\partial\overline{u}_j}{\partial x_i} - \frac{2}{3}\delta_{ij}\frac{\partial\overline{u}_k}{\partial x_k}\right) \tag{23}$$

with κ being the dynamic viscosity and δ_{ij} the Kronecker delta. Air compressibility has been demonstrated to influence the energy conversion process in small-scale OWC devices, particularly impacting the hydrodynamics of wave energy

Journal Pre-proof

absorption and the performance of the turbine [46]. Neglecting this factor may result in a considerable and unrealistic overestimation of the converter efficiency. Consequently, an ideal gas model is employed in this study [47].

$$p = \rho R T_0 \tag{24}$$

where R is the universal gas constant, and T_0 is the absolute temperature. The liquid tank experiences horizontal sinusoidal oscillations along the Ox_1-axis. The body force f_i consists of two components: the gravitational force in the vertical direction and the inertia force in the horizontal direction.

The turbine rotors are rotated passively by the reciprocating airflow. According to Newton's second law, the rotational motion of each rotor is governed by

$$J\dot{\omega} = T_\mathrm{a} - T_\mathrm{r} \tag{25}$$

where J represents the moment of inertia of a rotor, $\dot{\omega}$ represents angular acceleration, T_a represents the total driving torque due to the pressure difference across the rotor, and T_r refers to the reaction torque from the generator. The generator's reaction torque consists of inherent resistances and PTO effects. For simplification, T_r is considered proportional to ω as [48]

$$T_\mathrm{r} = \left(\mu + \mu_\mathrm{pto}\right)\omega \tag{26}$$

where μ and μ_pto are the inherent resistance and PTO damping coefficients, respectively. This linear simplification can accurately estimate the generated power in the mild-speed conditions considered in this study [49]. The PTO damping coefficient μ_pto is generated by the reaction force of the stator magnets. This occurs when the turbine rotor drives the generator rotor coil to cut magnetic flux lines for power generation. The value of μ_pto is related to the number of turns of the generator's coil and the magnetic field strength. In this study, μ_pto is considered a constant, with a unit $\mathrm{kg}\cdot\mathrm{m}\cdot\mathrm{s}^{-1}$. The power generated by each rotor can be calculated through

$$P(t) = \mu_\mathrm{pto}\omega^2 \tag{27}$$

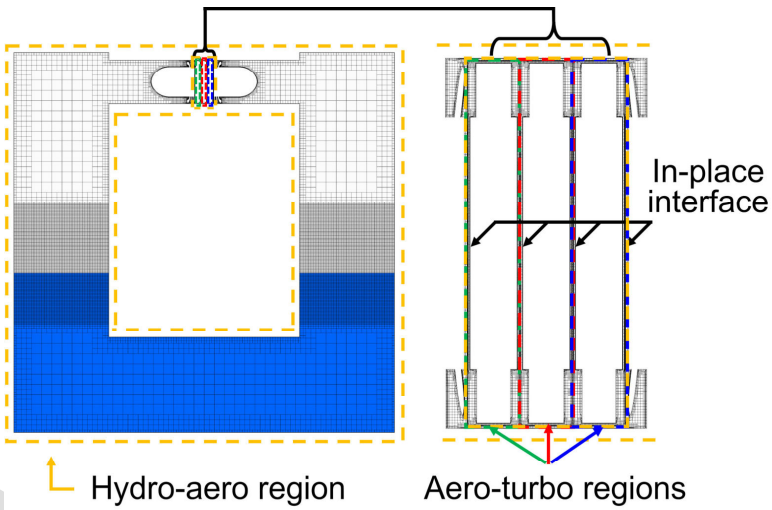


Figure 8: Illustration of hydro-aero and aero-turbo regions and zoomed-in view of aero-turbo regions

Journal Pre-proof

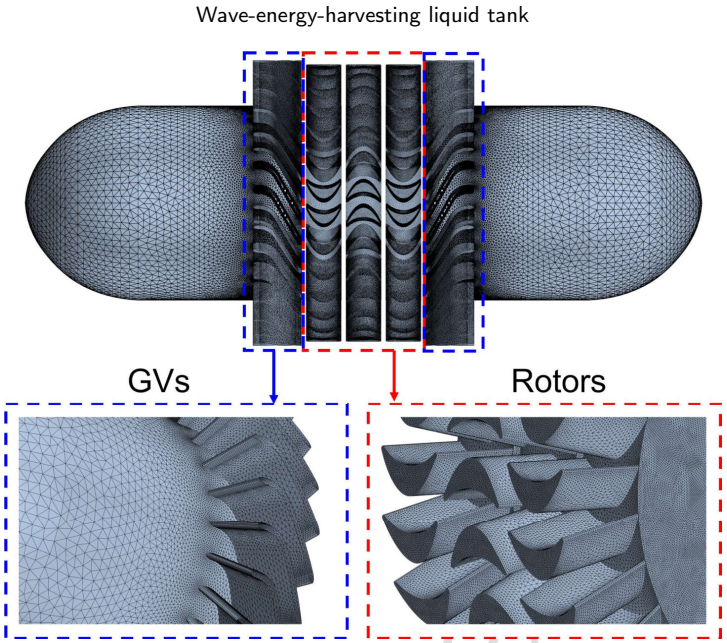


Figure 9: Surface mesh of multi-layered air turbine system

5.2. Detailed numerical techniques

The commercial computational fluid dynamics (CFD) software, StarCCM+, is used to implement the aforementioned mathematical process. The governing fluid equations are discretized by the finite volume method (FVM). The semi-implicit method for pressure linked equations (SIMPLE) scheme is employed as the pressure-velocity coupling algorithm in the solver. Reynolds-averaged Navier–Stokes (RANS) schemes were used. The turbulence closure was performed with the realizable k–ϵ mode. The second-order upwind scheme is employed to discretize the convection term. The free-surface motions inside the tank are captured using the High Resolution Interface Capturing (HRIC) method. The rotor motion is modeled using a single-degree-of-freedom dynamic-fluid-body-interaction (DFBI) rotation approach, in which an external damping torque is applied to represent the resistive moment acting on the rotor.

The whole computational domain is divided into a hydro-aero region and N aero-turbo regions, as shown in Fig. 8 . Here, N stands for the number of turbine rotors. For each rotor, two circular interfaces are set at its upstream and downstream, separating out an aero-turbo region. The hydro-aero region is the remaining area of the fluid domain after separating out N aero-turbo regions. Two adjacent regions share the same interface.

The in-place interface is a conformal, node-matching interface that enables a seamless connection between the hydro-aero region and the aero-turbo regions, or between adjacent aero-turbo computational regions. On one hand, it connects two regions within a single continuum, allowing the flow variables to be shared across them. On the other hand, it also manages the relative motion between the rotor and the stator of a turbo-machine. Notably, since no relative mesh movement occurs at the in-place interface, this approach significantly improves numerical stability, enables faster convergence, and achieves substantially higher computational efficiency—particularly in transient.

The rotor is initially defined as a continuum, a rigid body that can interact with the surrounding fluid through fluid-structure coupling. The motion of the rotor under aerodynamic forces is then captured by imposing rigid-body motion on the entire fluid mesh dynamic-fluid-body-interaction rotation (DFBI Rotation), thereby achieving two-way aero–turbo coupling.

Fig. 10 shows the procedure of the integrated numerical model. It is described in detail in Zhang et al. [50]. Through time marching, the angular velocity, denoted as ω, and angular displacement, ϕ, of each rotor are updated via the following implicit scheme:

$$\begin{aligned} \omega(t+\Delta t) &= \omega(t) + [\dot{\omega}(t) + \dot{\omega}(t+\Delta)]\Delta t/2 \\ \phi(t+\Delta t) &= \phi(t) + [\omega(t) + \omega(t+\Delta)]\Delta t/2 \end{aligned} \tag{28}$$

Journal Pre-proof

where Δt is the time step. Then, the calculation enters the loop at the $t + \Delta t$ step.

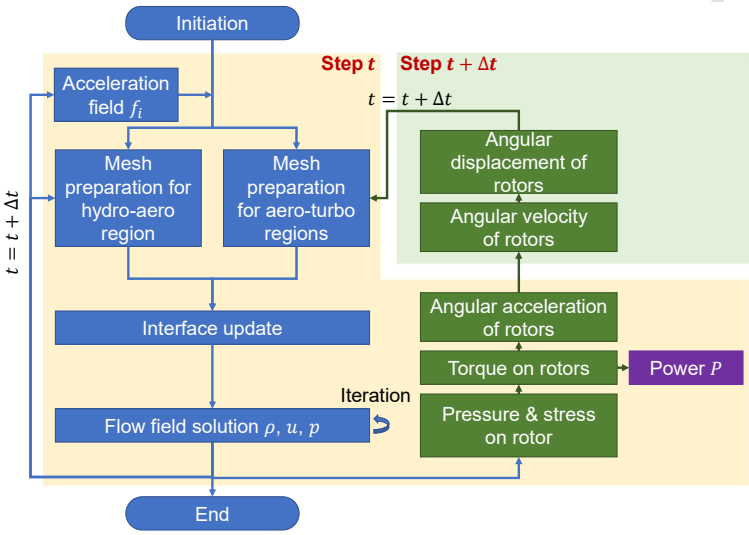


Figure 10: Flow chart of integrated numerical model for coupled hydro-aero-turbo dynamics of wave-energy-harvesting liquid tank

6. Results and discussion

6.1. Comparison between theoretical and experimental results

Fig. 11 compares the free-surface amplitude of the theoretical and experimental results for the liquid tank without a turbine. For the case without a turbine, the theoretical model does not include the "air model". The theoretical model can reasonably capture the trend of the liquid surface amplitude in relation to the excitation period T within the ranges of 0.95–1.10 s and 1.25–1.40 s. When varying the dimensionless coefficient representing the intensity of turbulent dissipation λ between 0.5 and 2.5, the resulting differences in η are relatively small, ranging from 1.00% to 5.80%. Therefore, a value of $\lambda = 1.5$ is chosen to represent the intensity of turbulent dissipation in the liquid tank.

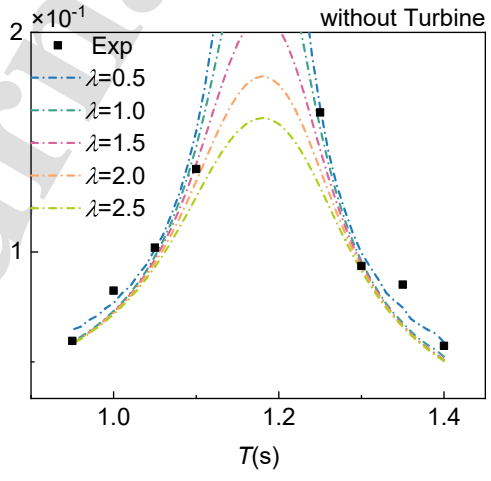


Figure 11: Comparison between theoretical and experimental results with Turbine-L1 for free-surface amplitude

Journal Pre-proof

Fig. 12 compares the theoretical and experimental results for the liquid tank without Turbine-L1. The free-surface amplitude and air pressure in the chamber are shown. The dimensionless turbulence coefficient c_t, which indicates the turbine's feature, is tuned. It shows that, for both the free - surface amplitude and the pressure drop, the theoretical results cannot match the experimental data under all excitation conditions. This is the case regardless of how the artificial tuning parameter c_t is adjusted. Meanwhile, the theoretical model slightly underestimates the liquid's natural frequency ω_1, with a deviation of 4.3%, as shown in Fig. 12 (a). It also underestimates the excitation period corresponding to the peak air pressure, with an error of 1.8%, as shown in Fig. 12 (b). Therefore, the theoretical model canot fully reflect the turbine's effects on the hydrodynamic or aerodynamic behavior of the liquid - tank system.

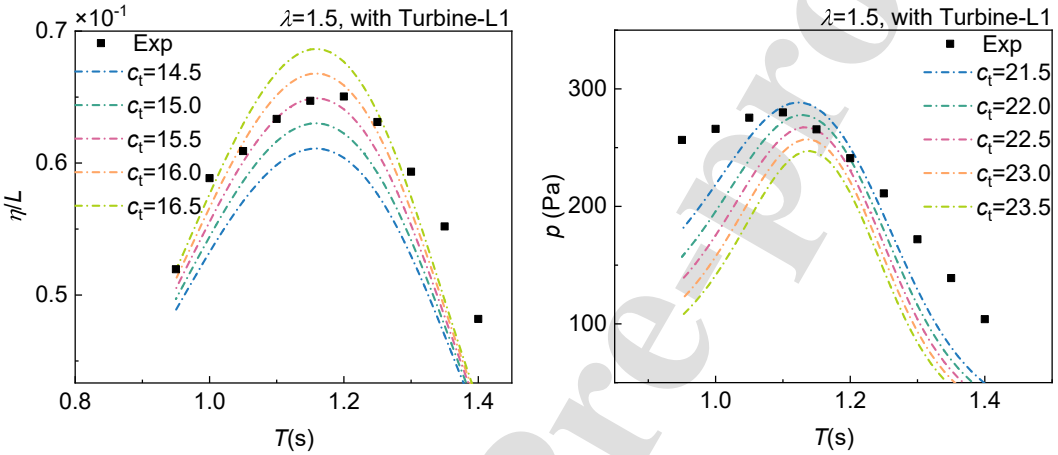


Figure 12: Comparison between theoretical and experimental results with Turbine-L1, for (a) free-surface amplitude; and (b) air pressure

6.2. Convergence study of integrated numerical model

The numerical mesh is generated for each region. Each mesh mainly consists of hexahedral cells, with the hydro–aero region comprising 3.13×10^6 cells and each aero–turbo region comprising 1.09×10^6 cells. Some trimmed polyhedral cells are used near fluid boundaries. Local mesh refinement is applied in both the air–water interface subzone and the air-duct subzone. In the air–water interface zone, the refined mesh has a length, width, and height of δx_1, δx_2, and δx_3, respectively, where $\delta x_1 = \delta x_2 < 1/10\ |\eta|$ and $\delta x_3 < 1/40\ |\eta|$ ($|\eta|$ denotes the free-surface amplitude), in order to accurately capture free-surface fluctuations. In the impulse turbine duct, the minimum width of the refined mesh is δx_4, which satisfies $\delta x_4 < 1/100\ l_d$, where l_d is the axial chord length of the rotor blade.

Further mesh refinement is applied to the guide vanes (GVs) and rotor blades within the air-duct subzone, as these regions typically represent the core zones of intense airflow variation, which is critical for ensuring numerical accuracy. Mesh refinement is not applied to the rotor hub region, since it is not located in the core turbulent area. This approach helps to reduce computational cost without significantly compromising accuracy.

On wall boundaries, prism layer meshes are applied in the direction normal to the wall boundaries, with a growth ratio of 1.2. The All $y+$ wall treatment model is employed to resolve both laminar and turbulent boundary layers effectively. The smallest mesh cell is found at the tip clearance of each rotor blade, with four grids arranged in the span-wise direction. The aero-turbo mesh moves with the rotor and is time-invariant relative to the rotor.

To ensure the accuracy of the proposed integrated numerical model for WEH liquid tanks, a convergence study is first conducted to determine spatial and temporal discretization. The model with Turbine-L1 is taken as an example. The moment of inertia J and the damping coefficient μ of the rotor are set as $J = 15J_0$ and $\mu = 4\mu_0$, respectively. Hereafter, for the convenience of expression, $J_0 = 1 \times 10^{-6}\text{kg}\cdot\text{m}^2$ and $\mu_0 = 1 \times 10^{-5}\text{kg}\cdot\text{m}^{-1}$ are used as units of measurement. The excitation period is $T = 1.10$s.

Four sets of numerical meshes with different grid densities are established for discretizing the fluid domain, as shown in Fig. 13. The four meshes have 2.94×10^6 ("mesh-1"), 3.47×10^6 ("mesh-2"), 4.21×10^6 ("mesh-3"), and

Journal Pre-proof

5.66×10^6 ("mesh-4") cells, respectively. From mesh-1 to mesh-4, the mesh grids near the free surface and the turbine system are refined. This refinement is strategically carried out to track the dynamic behaviour of the free surface and capture the flow details during the interaction between the air and the turbine system.

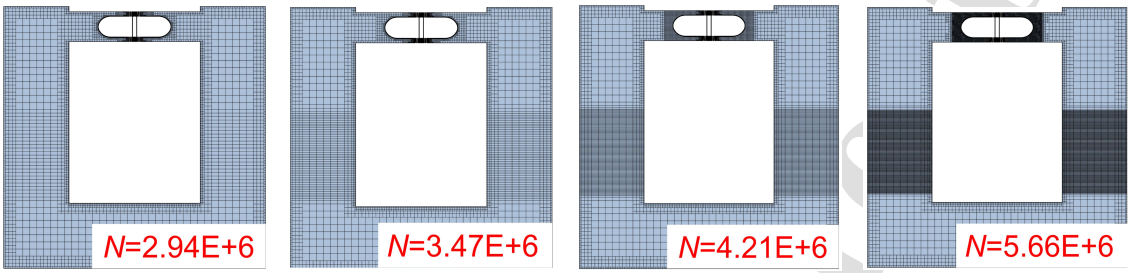


Figure 13: Mesh models for spatial convergence study: (a) mesh-1; (b) mesh-2; (c) mesh-3; and (d) mesh-4

Fig. 14 (a) shows the calculated time histories of the rotor speed, the free-surface elevation, and the pneumatic pressure in the right-hand-side air chamber. The time step is set as small as Δt =0.0002s. The unit of rotor speed is revolutions per second (rps) hereafter.

All four sets of meshes can lead to stable results. Although the differences in results between any two meshes are small enough, it is still clear that the results converge quickly as the number of mesh cells increases. As the grid number increased from 2.94×10^6 to 4.21×10^6, the variations in rotor speed n, free-surface elevation amplitude η, and pneumatic pressure p decreased by 0.74%, 1.33%, and 0.54%, respectively. With a further increase to 5.66×10^6, changes in n, η, and p became negligible, with the maximum variation not exceeding 0.56%. These results indicate that the numerical solution had reached a stable level of convergence. Therefore, a grid number of 4.21×10^6 ("mesh-3")was adopted to ensure computational efficiency without compromising accuracy.

Based on mesh-3, convergence studies are further conducted for the time step. Three different time steps are considered, with $\Delta t = 0.0002$s, 0.001s, and 0.002s, respectively. Accordingly, the calculated time histories of the rotor speed, the free-surface elevation, and the pneumatic pressure are shown in Fig. 14 (b). Compared to the free-surface elevation and pneumatic pressure, the rotor speed is more sensitive to the time step. When the time step was reduced from 0.002 s to 0.001 s, the rotor speed n, free-surface elevation amplitude η, and pneumatic pressure p increased by 7.87%, 2.36%, and 2.84%, respectively. Further reduction of the time step to 0.0002 s resulted in maximum variations of less than 2.16% in these parameters. Considering the computational cost, a time step of 0.001 s was deemed acceptable.

6.3. Comparison between numerical and experimental results

The numerical results are compared with the experimental data to further validate the integrated numerical model. The excitation condition of $T = 1.10$s is shown here as an example. Figs. 15 (a)-(e) illustrate snapshots of the free-surface profile in the WEH liquid tank without the turbine system at $t = 10.6$s, $t = 10.7$s, $t = 10.8$s, $t = 10.9$s, and $t = 11.0$s respectively. Meanwhile, Figs. 15 (f)-(j) show the numerical results at the corresponding instants. For the liquid behaviour, the numerical results agree well with the experimental observations at all instants. The present numerical model can reproduce even the slight free-surface breaking phenomenon under this excitation condition. Figs. 16 (a)-(e) further illustrate snapshots of the free-surface profile in the tank with Turbine-L1 at t = 10.6s, 10.7s, 10.8s, 10.9s, and 11.0s respectively. Figs. 16 (f)-(j) show the numerical results at the corresponding instants. It can be observed that the present integrated numerical method can also reproduce the liquid behaviour well at all times.

Fig. 17 further compares the experimental results with the numerical results for more excitation conditions with T =1.00s, 1.05s, 1.10s and 1.15s. Figs. 17 (a), (b), and (c) refer to the rotor speed, the free-surface elevation, and the pneumatic pressure in the right-hand-side air chamber, respectively. In the steady stage of each excitation condition, the numerical results always agree well with the experimental data with sufficient accuracy. Especially for the free-surface elevation, the experimental results and the numerical results are almost identical. Based on the aforementioned observations, it can be confirmed that the present integrated numerical model can provide reliable results that accurately reflect the physical reality.

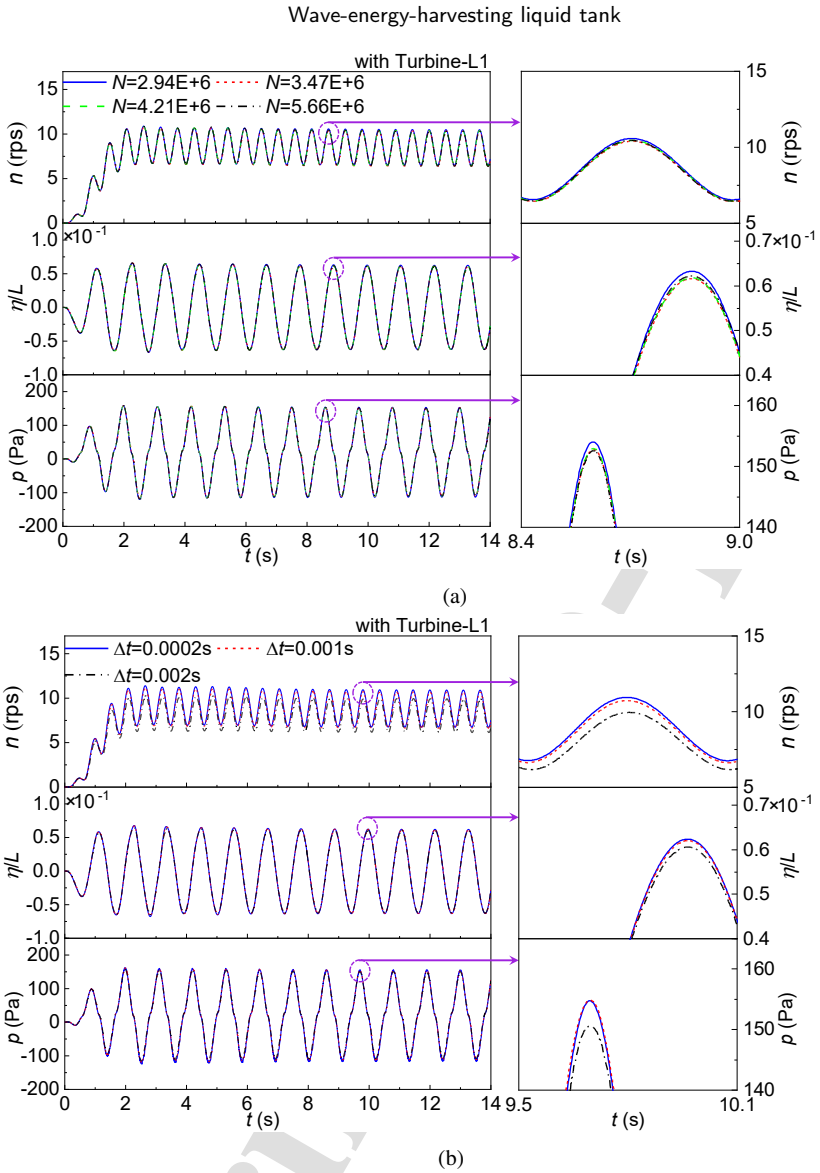


Figure 14: Convergence study for (a) mesh discretization, and (b) time step

6.4. Analyses of mechanical parameters of turbine rotor

According to Eq. (27), the rotational behaviour of the turbine rotor is a key factor determining the power output of a WEH liquid tank. For each rotor, the moment of inertia J and the damping coefficient μ are inherent dynamic parameters that can affect its rotational behaviour. Before investigating the power conversion properties of a WEH liquid tank, this subsection first discusses the effects of J and μ on rotor speed.

Fig. 18 gives an example of the rotor speed history, when the tank is excited at $T = 1.10$s. The rotor has $J = 15J_0$ and $\mu = 4\mu_0$. The upper and lower limits of the rotor-speed variation are nearly time-invariant. The value of n_{ave} represents the mean of the upper and lower limits. Subtracting n_{ave} from n results in the oscillatory component n_{osc}. The oscillatory component in the steady stage is nearly sinusoidal and has an almost constant amplitude. Half the difference between the upper and lower limits of n_{osc} can be defined as the variation range of the rotor (denoted as

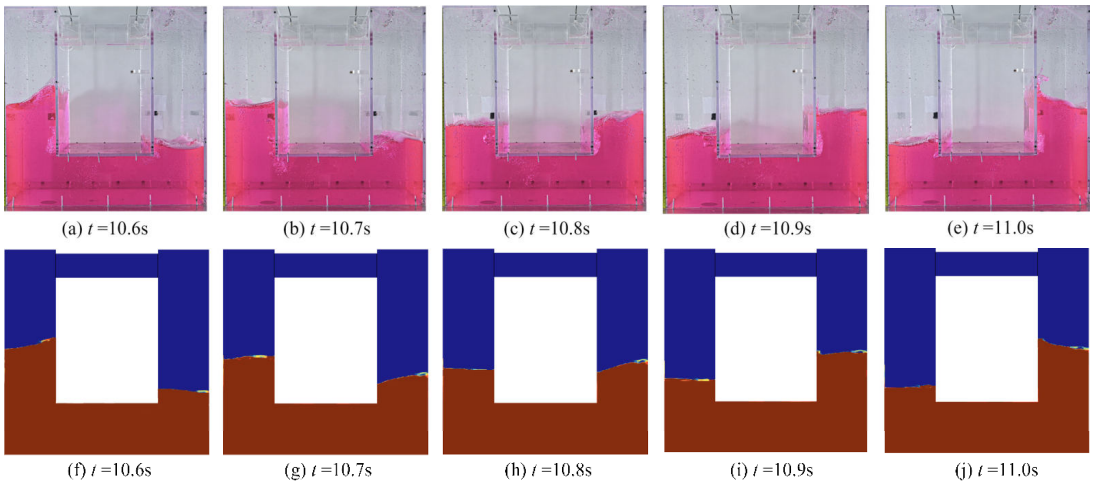


Figure 15: Comparison of experimental snapshots at t= (a) 10.6s, (b) 10.7s, (c) 10.8s, (d) 10.9s, and (e) 11.0s with numerical results at t= (f) 10.6s, (g) 10.7s, (h) 10.8s, (i) 10.9s, and (j) 11.0s, for wave-energy-harvesting tank without turbine in excitation condition of T=1.10s

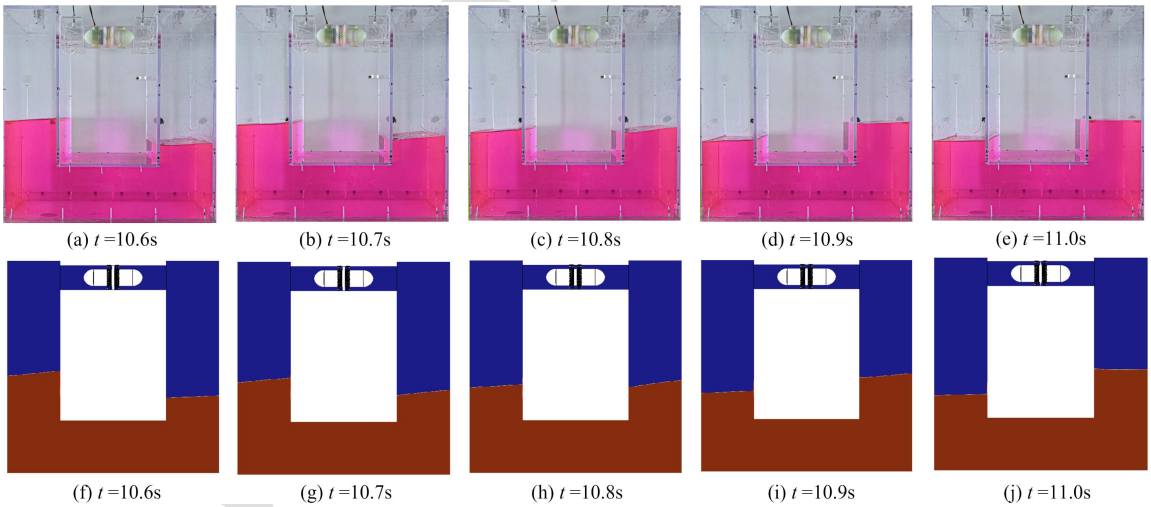


Figure 16: Comparison of experimental snapshots at t= (a) 10.6s, (b) 10.7s, (c) 10.8s, (d) 10.9s, and (e) 11.0s with numerical results at t= (f) 10.6s, (g) 10.7s, (h) 10.8s, (i) 10.9s, and (j) 11.0s, for wave-energy-harvesting tank with Turbine-L1 in excitation condition of T=1.10s

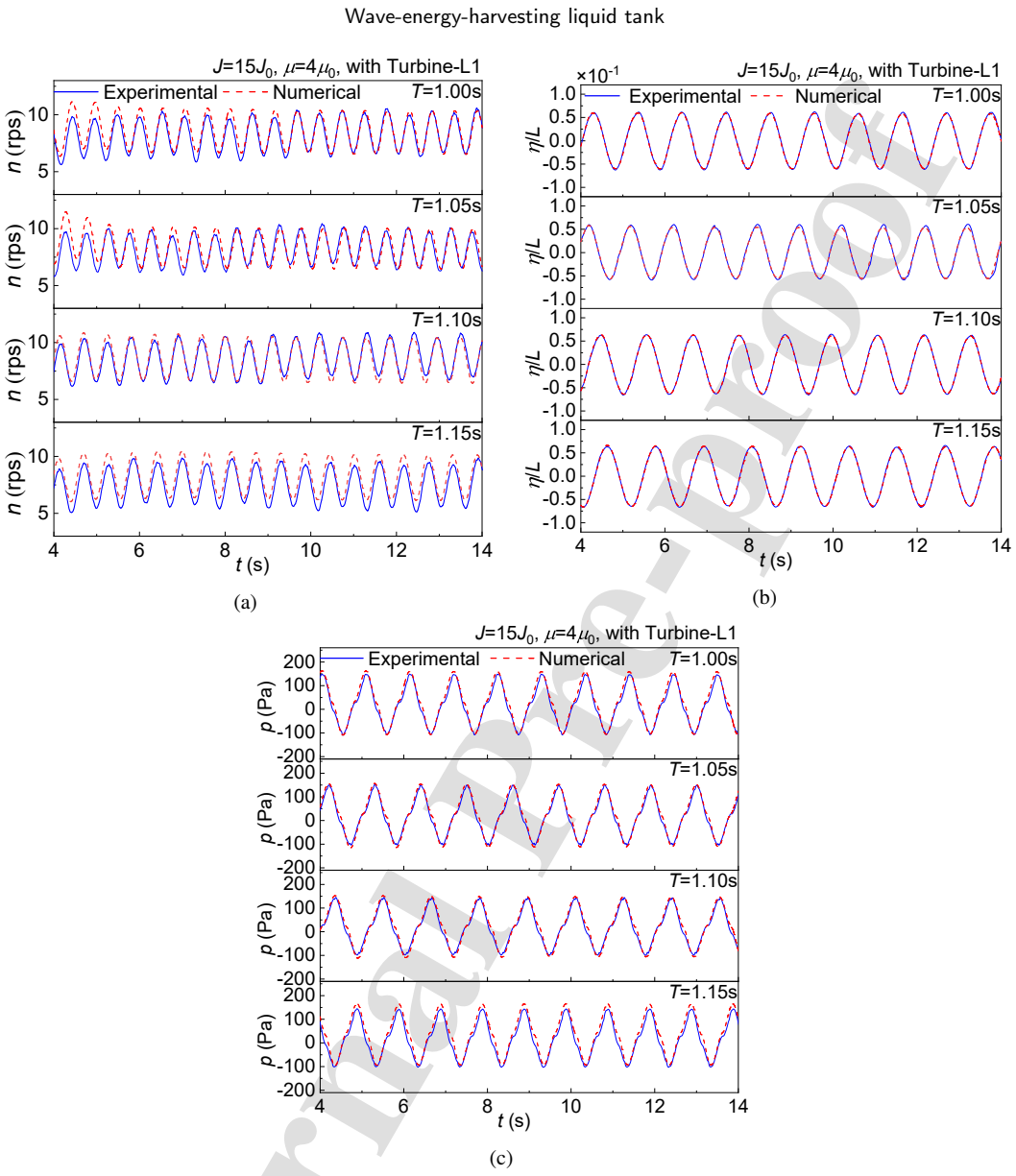


Figure 17: (a) Validition of rotor speed (b) validiton of liquid surface displacement; (c) validiton of pressure

$|n_{osc}|$). In the steady stage of this case, the averaged rotor speed is about $n_{ave} = 8$ rps. The maximum speed is 11 rps, and the minimum speed is 5 rps. Therefore, the variation range is $|n_{osc}| = 3$ rps.

Fig. 19 (a) illustrates the effects of the moment of inertia on the rotor speed. The value of J varies from $10J_0$ to $20J_0$, while the damping coefficient remains constant with $\mu = 4\mu_0$. For cases with $J = 10J_0$, $15J_0$, and $20J_0$, the averaged speed of the rotor is almost identical in all these excitation conditions. From $T = 0.80$ s to 1.10 s, the average rotor speed increases slowly from about 7 rps to over 8 rps. The maximum averaged rotor speed appears at $T = 1.10$s. In even larger excitation periods, the averaged speed decreases monotonically from $T = 1.10$ s to $T = 1.40$ s, down to 3 rps. In Fig. 19 (b), the variation ranges corresponding to the three moments of inertia are explicitly compared. The variation ranges of the rotors also first increase with the excitation period, reach the maximum at $T = 1.10$ s, and

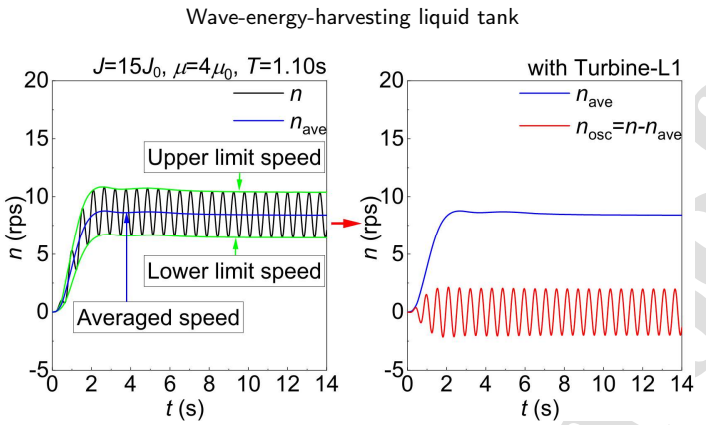


Figure 18: History of rotor speed and its decomposition

then decrease monotonically. An increase in the rotor moment of inertia from $10J_0$ to $20J_0$ results in a reduction of approximately 46.32% in the variation range of the rotor speed.

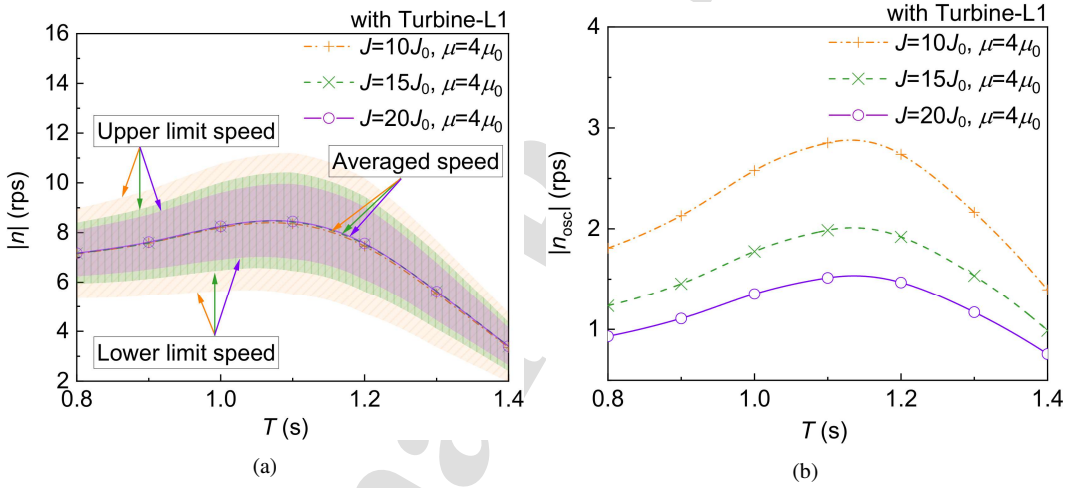


Figure 19: Effect of moment of inertia on rotor speed: (a) averaged rotor speed and speed limits; (b) variation range of rotor speed

Fig. 20 shows the effects of the damping coefficient on the rotor speed. The moment of inertia remains constant, with $J = 15J_0$. From Fig. 20 (a), it can be told that as the damping coefficient reduces from $\mu = 6\mu_0$ to $\mu = 2\mu_0$, the maximum averaged rotor speed increases from 6 rps up to over 13 rps. A decrease in the damping coefficient μ from $6\mu_0$ to $4\mu_0$ results in an approximate 41.63% increase in the averaged rotor speed. Further reducing μ to $2\mu_0$ (equivalent to 33.33% of $6\mu_0$) lead to the averager rotor speed reaching approximately 2.44 times its original value at $6\mu_0$. Fig. 20 (b) compares the variation ranges of the rotor speed that correspond to three damping coefficients. From $\mu = 2\mu_0$ to $\mu = 4\mu_0$, the maximum variation range increases from about 1.8 rps to 2.0 rps, by approximately 11.11%. However, when μ increase from $4\mu_0$ to $6\mu_0$, the increment is only around 3.00%.

6.5. Identification of optimal power take-off damping for wave energy harvesting

The PTO damping of the turbine rotor is a crucial parameter that determines the amount of wave energy harvested. Fig. 21 shows an example of the real-time power output $P(t)$ of the WEH liquid tank with Turbine-L1. The excitation period is $T = 1.1$s, the moment of inertia of the rotor is $J = 15J_0$, the damping coefficient of the rotor is $\mu = 4\mu_0$, and the PTO damping is $\mu_{\text{pto}} = 5\mu_0$. The power output $P(t)$ increases in a fluctuating manner from zero and eventually

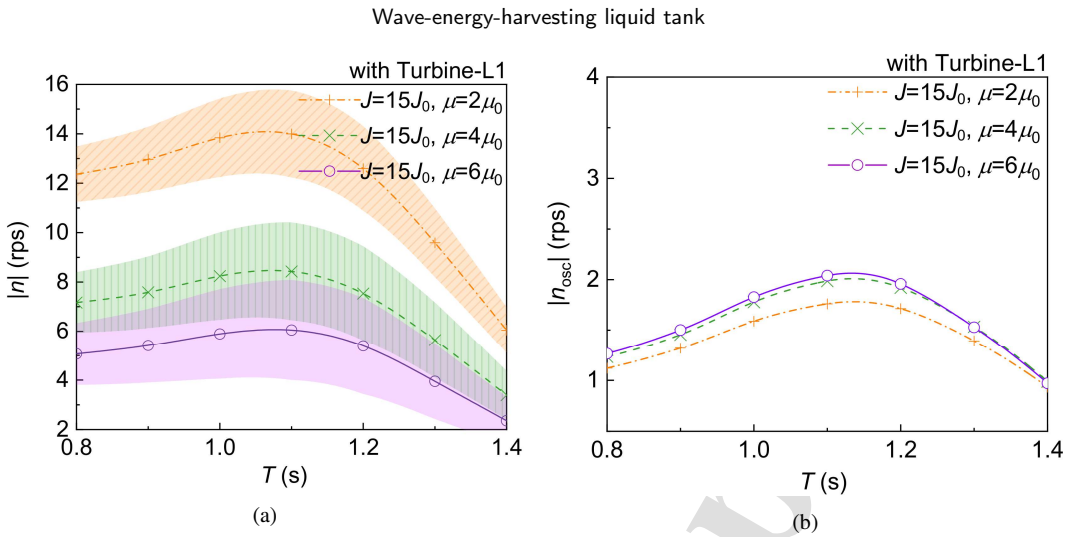


Figure 20: Effect of damping coefficient on rotor speed: (a) averaged rotor speed and speed limits; (b) variation range of rotor speed

stabilizes in a steady stage with a nearly constant maximum amplitude. The averaged power P_{ave} in the steady stage can be calculated as follows:

$$P_{\text{ave}} = \frac{\int_{t_0}^{t_0+mT} P(t)\mathrm{d}t}{mT} \tag{29}$$

where t_0 can be any moment in the steady stage, m represents the number of periods to be considered, and T is the excitation period.

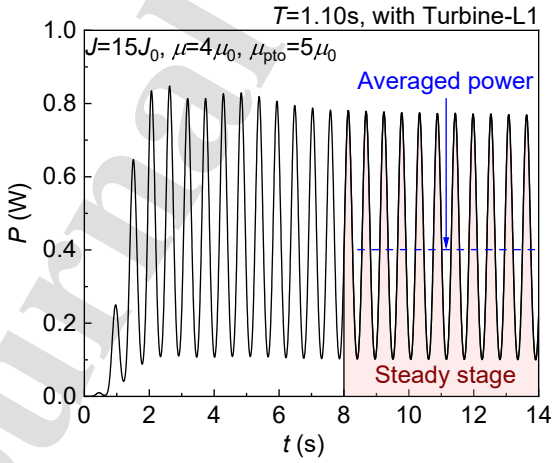


Figure 21: History of generated power of wave-energy-harvesting liquid tank

Fig. 22 shows the effects of the PTO damping on the averaged power output, the amplitude of free-surface oscillation, the averaged rotor speed, and the variation range of the rotor speed for the WEH liquid tank with Turbine-L1 under various excitation periods. The PTO damping μ_{PTO} varies from 0 to $10\mu_0$. From Fig. 22 (a), an optimal region of working conditions can be found for power harvesting. The optimal region is formed from $T = 0.80$ s to 1.25 s and from $\mu_{\text{PTO}} = 2.0\mu_0$ to $10\mu_0$. The maximum averaged power is approximately 0.4W near the condition with $T = 1.10$

Journal Pre-proof

s and $\mu_{\mathrm{PTO}} = 6.0\mu_0$. Beyond the optimal region, when T increases from 1.2s to 1.4s, or when μ_{PTO} decreases from $2.0\mu_0$ to $0\mu_0$, the averaged power output continuously decreases from around 0.2W. Fig. 22 (b) indicates that the PTO damping does not affect the free-surface oscillation amplitude evidently under any excitation period. With a specific PTO damping, the free-surface amplitude first increases with the excitation period from $T = 0.80$ s to around 1.15 s and then decreases with the period. The maximum free-surface amplitude occurs around $T = 1.15$s, close to the resonant period of the liquid in the U-shaped tank. It is known that the oscillation of the liquid body is the source of turbine rotations and power conversion. For Turbine-L1, changing the PTO damping of the single rotor has little impact on the free-surface amplitude. This indicates that the harvested and dissipated energy of Turbine-L1 accounts for a small proportion of the liquid mechanical energy, with a value of less than 40%. There is still great potential to harvest the liquid-motion energy in the WEH liquid tank by improving the turbine system. According to Fig. 22 (c), the maximum averaged rotor speed exceeds 8 rps, which appears in the condition of around $T = 1.05$ s and $\mu_{\mathrm{PTO}} = 0$. Under each excitation period, the averaged rotor speed decreases as the PTO damping increases. The averaged rotor speed is between 2 and 6 rps in the optimal region. In larger period conditions beyond $T = 1.20$ s, the averaged rotor speed decreases rapidly,with a reduction of approximately 50% or more. Even with $\mu_{\mathrm{PTO}} = 0$, the averaged rotor speed is only about 3 rps at $T = 1.14$ s. Fig. 22 (d) shows the variation range of the rotor speed. The maximum variation range is about 2 rps. It appears in the region formed from $T = 1.10$ s to 1.20 s and from $\mu_{\mathrm{PTO}} = 0$ to μ_0. Outside this region, the PTO damping does not have much impact on the variation range of the rotor speed.

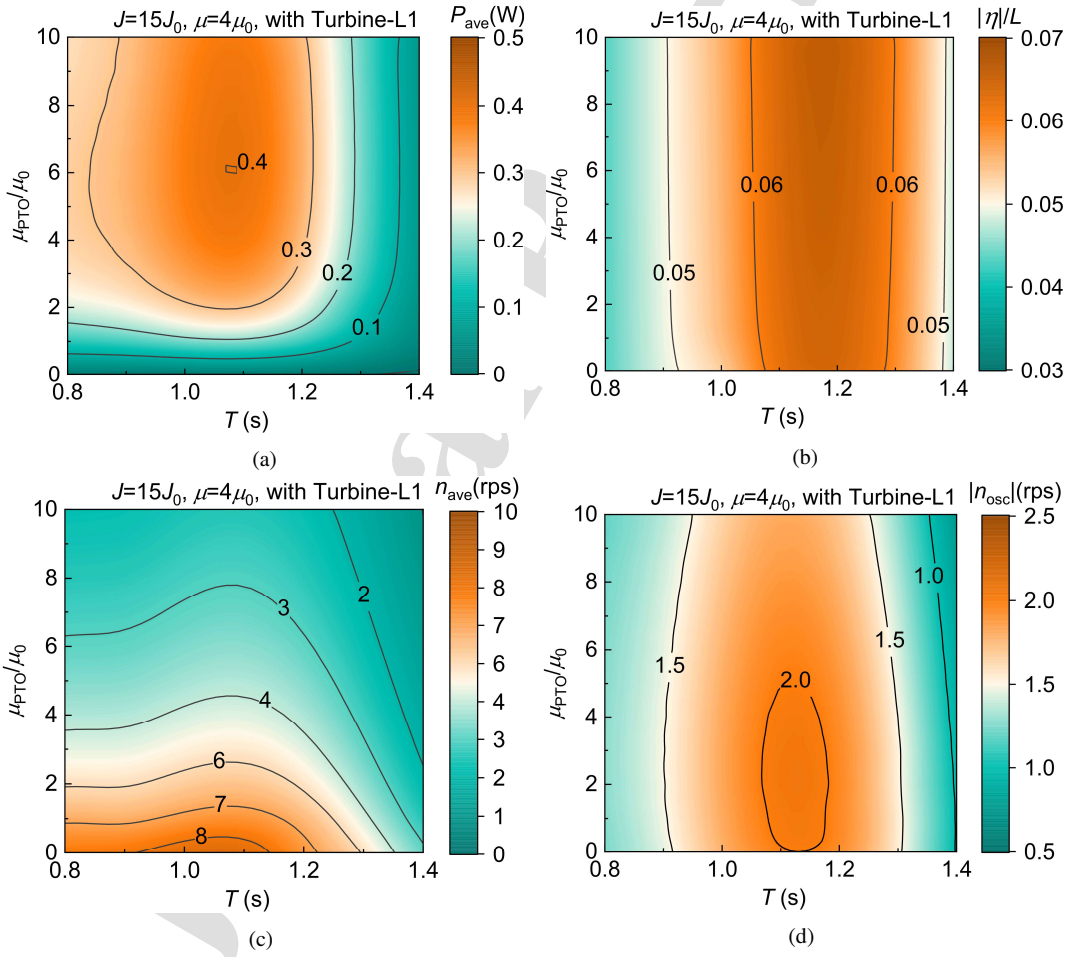


Figure 22: Effect of power take-off damping on (a) averaged power, (b) free-surface amplitude, (c) averaged rotor speed, and (d) variation range of rotor speed

Journal Pre-proof

6.6. Efficiency performance of multi-layered impulse air-turbine system

This subsection compares the performance of the other two MLATSs, namely Turbine-L2 and Turbine-L3, with that of Turbine-L1. The design details of the three turbines are introduced in Fig. 5. According to the parametric studies in subsections 6.4 and 6.5, the following optimal parameters are set for each rotor: $J = 15J_0$, $\mu = 4\mu_0$, and $\mu_{\mathrm{PTO}} = 5\mu_0$.

The excitation condition with $T = 1.10$s is considered for illustration purposes. Fig. 23 (a) shows the power output histories of each rotor and the power summation of two rotors for Turbine-L2. When the upstream rotor reaches its larger power peak at 0.68 W, the downstream rotor reaches its lower power peak at 0.20 W simultaneously. The summation of the power histories reveals a steady power amplitude, which is similar to the power history of Turbine-L1 in Fig. 21. Fig. 23 (b) shows the power output histories of each rotor and the power summation of three rotors for Turbine-L3. In the steady stage, during each excitation period, the power output history of Rotor-1 or Rotor-3 alternately shows a larger peak at 0.52 W and a smaller peak at 0.18 W. Rotor-2 has a steadier yet much smaller amplitude of power output compared with the other two rotors, approximately 0.15 W.

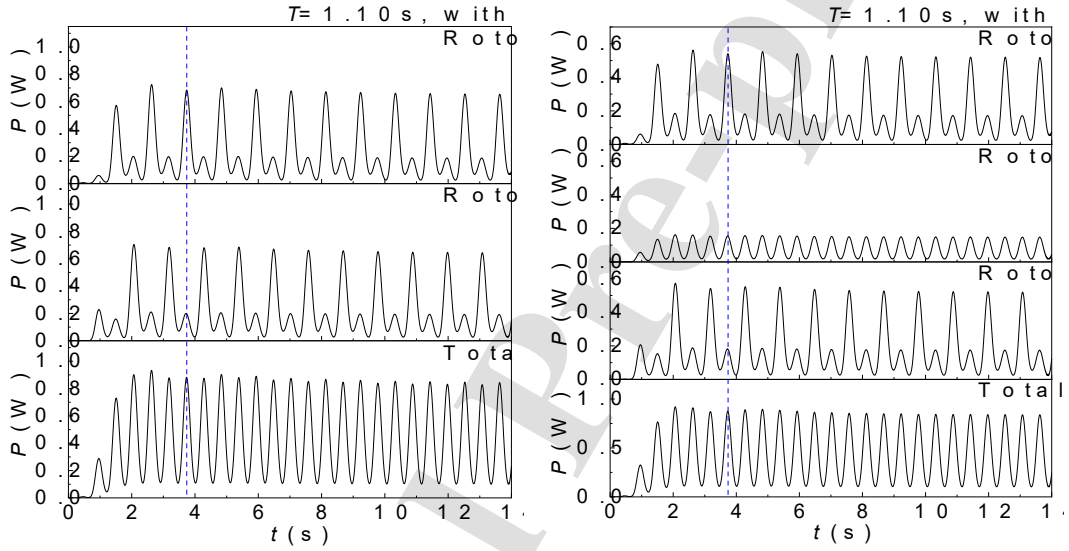


Figure 23: Power output histories of rotors in wave-energy-harvesting liquid tank with (a) Turbine-L2 and (b) Turbine-L3, for $T = 1.10$s

Fig. 24 illustrates the amplitude distribution and the vector field of the air-flow velocity near the turbine system. At the same instant, the velocity amplitude distributions near Turbine-L1, Turbine-L2, and Turbine-L3 display similar patterns. The upstream vector field in front of each turbine is fairly uniform, and the average airflow velocity is approximately 15 m/s. Vortices of similar size can be seen at the downstream side of each turbine.

Fig. 25 (a) compares the total averaged power outputs of Turbine-L1, Turbine-L2, and Turbine-L3. All three turbines have their maximum averaged power appear in the excitation condition of $T = 1.10$s. The largest power output is $P_{\mathrm{ave}} = 0.45$ W. For excitation conditions with $T > 1.10$s, improving Turbine-L1 to Turbine-L2 or Turbine-L3 does not increase the averaged output of the WEH liquid tank evidently, yielding average gains of merely 8.20% and 8.18%, respectively. Under conditions of smaller-period excitation, the averaged power output clearly increases from Turbine-L1 to Turbine-L3, with the average improvement reaching 14.59% and 29.44%, respectively. In the excitation condition where $T = 0.80$ s, if Turbine-L2 is used, the averaged power output of Turbine-L1 increases by about 25%. Meanwhile, if Turbine-L3 is used, the increase ratio is about 40%. Fig. 25 (b) shows the free-surface oscillation amplitude in the liquid tank when Turbine-L1, Turbine-L2, and Turbine-L3 are used, respectively. As the number of rotors increases from one to three from Turbine-L1 to Turbine-L3, the free-surface amplitude decreases accordingly. From the energy perspective, the energy loss of the liquid motion mainly results from two factors: One is energy dissipation, and the other is energy absorption by the turbine system. By comparing the results of $T > 1.10$ s in Figs. 25 (a) and (b), it

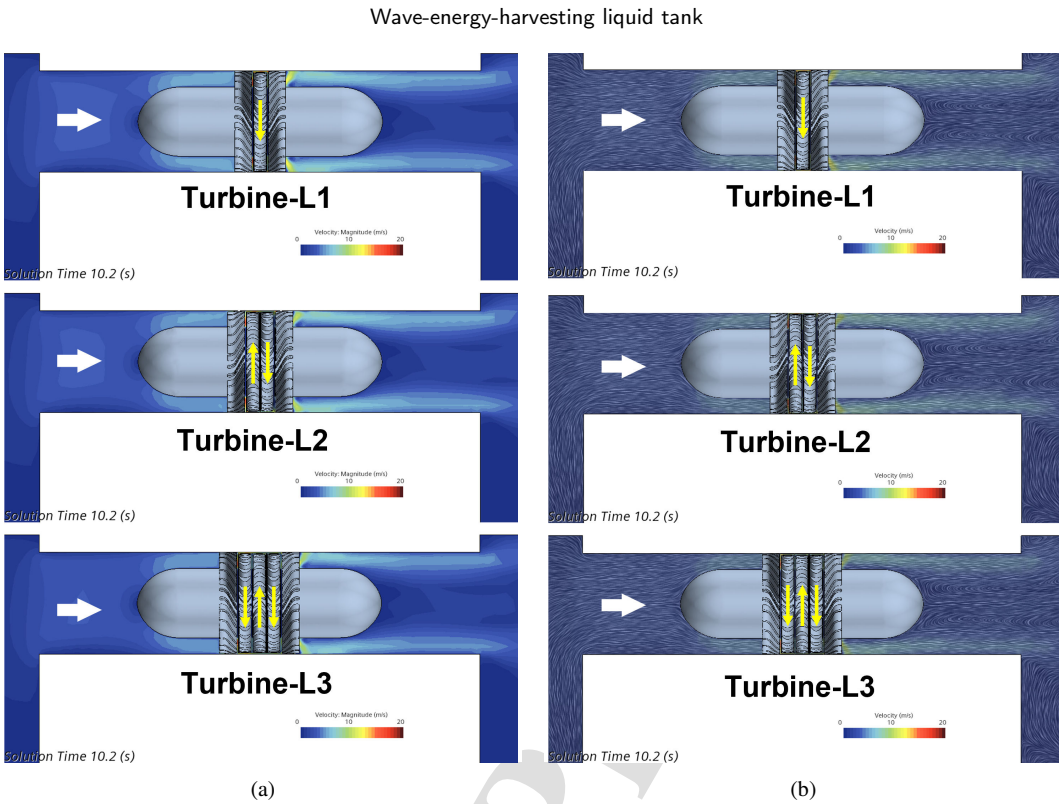


Figure 24: (a) Amplitude distribution and (b) vector field of air-flow velocity near the turbine system, in excitation condition of $T = 1.10$s

can be understood that Turbine-L3 and Turbine-L2 dissipate more energy than Turbine-L1 under these large-period conditions.

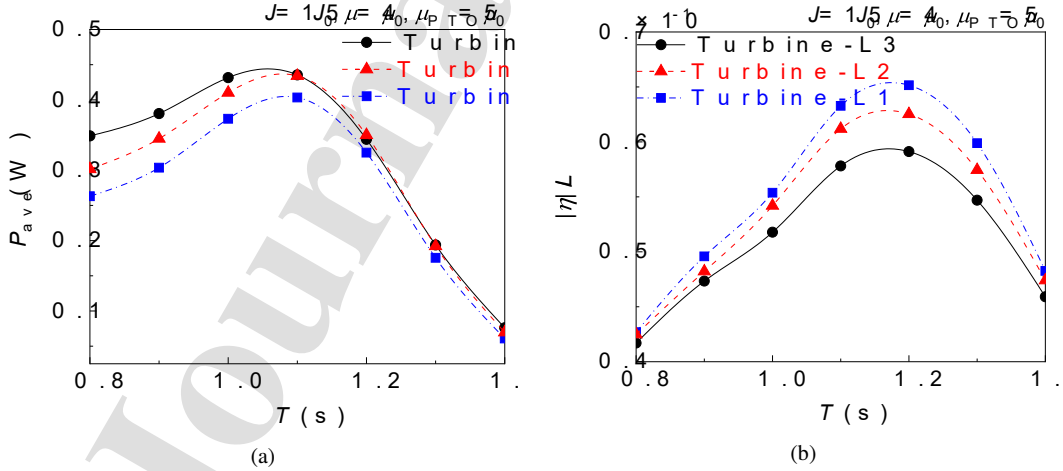


Figure 25: (a) Averaged power outputs, and (b) free-surface amplitudes in wave-energy-harvesting liquid tank with Turbine-L1, Turbine-L2 and Turbine-L3

Journal Pre-proof

6.7. Reliability analyses of multi-layered impulse air-turbine system

Regarding reliability liquid-tank En-WECs, because of the gyroscope principle, in harsh sea states, the axis of the rotating turbine constantly experiences strong dynamic bending moments. Going offshore to retrieve the device for maintenance often costs more than the WEC device. This subsection aims to analyze the reliability of Turbine-L3 through a series of failure tests. The cases are referred to by using the index system $i-j-k$. Here, the indices i, j, and k correspond to the status of Rotor-1, Rotor-2, and Rotor-3, respectively. If Rotor-i is damaged, $i = 0$; Otherwise, $i = 1$. Four failure cases, namely case 0-1-1, case 1-0-1, case 0-0-1, and case 0-1-0, are considered as examples. A damaged rotor has zero PTO damping and thus does not generate power. Case 1-1-1 refers to the status when the turbine works well and all three rotors are healthy. Fig. 26(a) shows the rotor speed status of case 0-1-1 when Rotor-1 is damaged. Fig. 26(b) refers to the status when Rotor-2 fails. Fig. 26(c) corresponds to the situation where both Rotor-1 and Rotor-2 are damaged. In Fig. 26(d), both Rotor-1 and Rotor-3 are damaged at the same time. Each damaged rotor can rotate freely without the PTO damping. In all these failure cases, the maximum rotor speed of a damaged rotor increases by approximately 2 to 3 rps compared to its healthy status. Moreover, the failure of any rotor does not affect the rotor speeds of the undamaged rotors. This observation confirms that Turbine-L3 is inherently robust to adapt to damage accidents.

Fig. 27 further compares the averaged power output of these four failure cases. It reveals that the failure of Rotor-2 has the least impact on the total power generation. Compared with the healthy status, the average power output in case 1-0-1 is only reduced by 22%. This power generation capability is still quite close to that of Turbine-L1. If either Rotor-1 or Rotor-3 fails to work, the turbine's power generation capability can drop by about 44%. When both Rotor-1 and Rotor-2 are damaged, Turbine-L3 remains at 38% of its rated capability. In the worst case when only Rotor-2 works, the power output of Turbine-L3 is reduced to 14% of its rated capability. This suggests that the contribution of the two side rotors (Rotor-1 or Rotor-3) to the power output is greater than that of the middle rotor (Rotor-2). The aforementioned analyses confirm that Turbine-L3, a MLATS, is far more reliable in extreme conditions than a conditional turbine with a single rotor.

7. Further discussion

This section briefly summarizes the key contributions of this study for readers to review. First, this study proposes an integrated numerical model that is coupled with real turbine motions for liquid-tank En-WECs. With this approach, complex turbine effects in liquid-tank En-WECs can be directly simulated. Second, this study provides benchmark experimental data that can be directly used to validate the theoretical or numerical models of the liquid tank with the air-turbine system. This fills an important gap in the benchmark experimental database for liquid-tank En-WECs. Third, this study creatively examines a strategy of integrating an MLATS into the liquid-tank En-WEC. Compared to a conventional single-rotor turbine, the MLATS shows enhanced efficiency and reliability. The MLATS strategy essentially indicates an innovative way to solve the weaknesses of conventional liquid-tank En-WECs.

A comprehensive commentary can be made on the obtained results in Sec. 6. Under the examined excitation conditions, the moment of inertia of the rotor exhibits negligible influence on the average rotational speed; however, it significantly affects the amplitude of speed fluctuations. Conversely, the damping coefficient exerts a pronounced impact on the average rotational speed, while its influence on the fluctuation amplitude remains minor. The optimal PTO damping for the WEH liquid tank is also identified. For a WEH liquid tank that is as small as 0.6m long, the maximum averaged power is around 0.4W near the resonance condition. Each of the three turbines has its maximum averaged power appearing near the resonance condition of the liquid tank.

The concept of the present WEH liquid tank is essentially a fully enclosed OWC device. The conventional OWC devices are well-known for their advantages like simple structure, reliability, and low maintenance cost. They are suitable for nearshore applications, low-to-medium wave conditions, and integration with coastal infrastructure. A typical established OWC technology can be found in Henriques et al. [51] for the Mutriku wave power plant, in which a detailed analysis of the dynamics and control of air turbines and electrical generators in OWCs was provided. In severe sea states, as a "fully - enclosed" OWC, it is expected that the present WEH liquid tank with an air-turbine system has distinct advantages in survivability and durability.

It should be noted that this study adopted relatively mild wave conditions. This is mainly because the physical model experiments aimed to calibrate the integrated numerical model. The calibration requires accurate measurements of the free-surface displacements. Under more severe conditions, surface breaking often occurs during most excitation periods. Since the enclosed air chamber provides an air-spring effect, the airflow through the air turbine system is

Journal Pre-proof

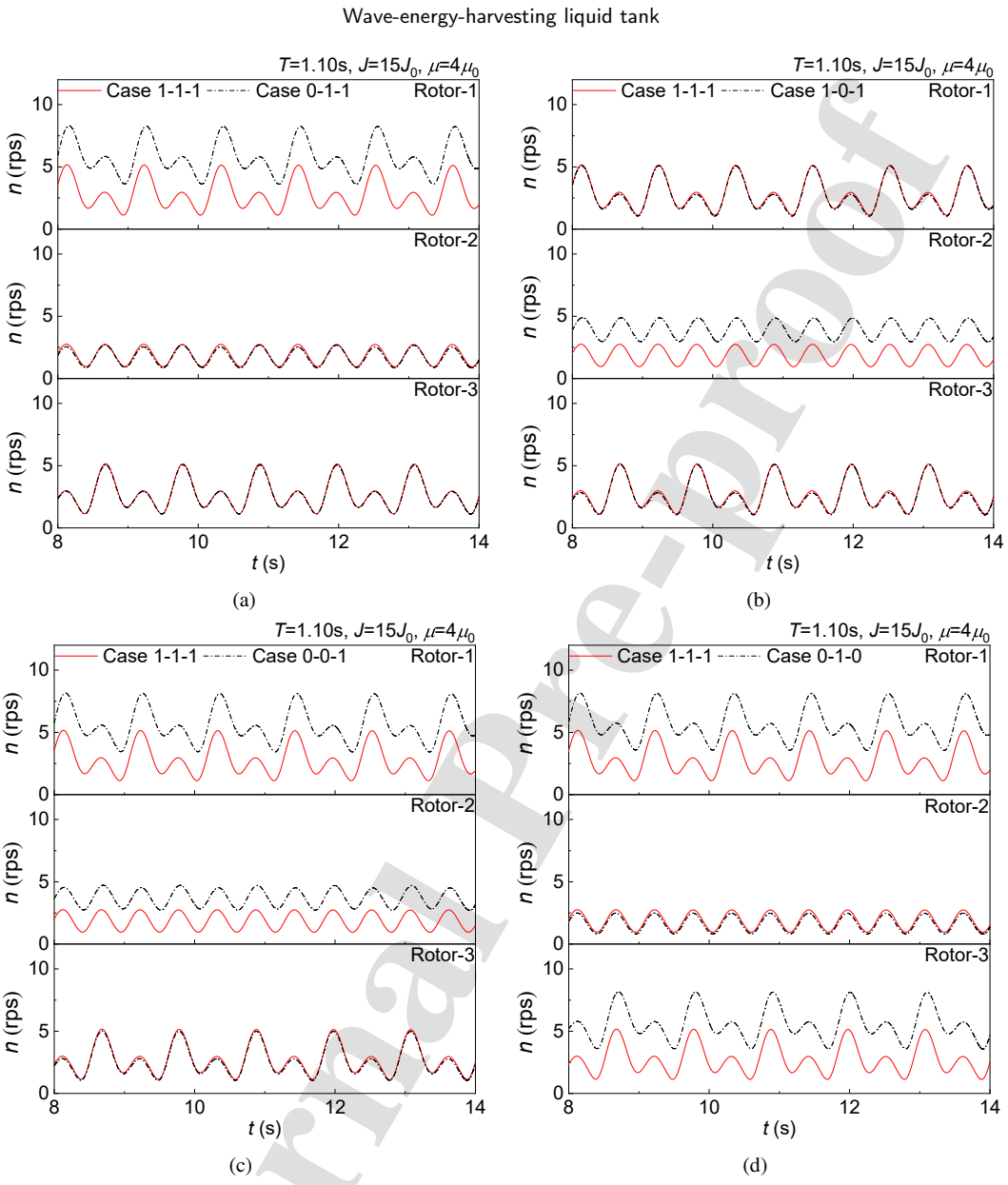


Figure 26: Rotor speed status of Turbine-L3, in failure cases of (a) 0-1-1, (b) 1-0-1, (c) 0-0-1, and (d) 0-1-0

expected to stay stable and relatively smooth. The aerodynamic pressure in the sealed liquid tank may be less sensitive to free-surface breaking phenomena. Future work should further explore the system's performance under extreme wave conditions.

Due to the paper's length limit, more detailed descriptions and case studies for the WEH liquid tank can be found in Zhang et al. [50].

Journal Pre-proof

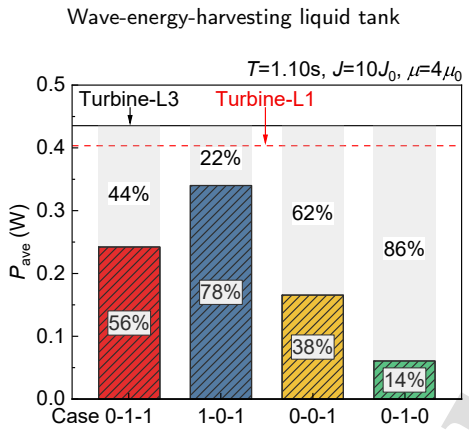


Figure 27: Capability loss of Turbine-L3 in different failure cases

8. Conclusions

This study proposes an integrated numerical model to couple with actual turbine motions. A series of experiments are conducted on a prototype of the WEH liquid tank with an impulse air turbine system. Benchmark experimental data are obtained for validation of the numerical model. The proposed integrated numerical model accurately reproduces the experimental observations. The effects of turbine parameters on the coupled hydro-aero-turbo behavior are systematically investigated. For the considered excitation conditions, the moment of inertia of a rotor mainly affects the variation range of the rotor speed evidently. The damping coefficient markedly influences the averaged rotor speed, but has little effect on the variation range of the rotor speed. The optimal power take-off damping for the WEH liquid tank is identified. A multi-layered impulse air turbine system (MLATS) is creatively introduced into the liquid-tank system to explore its capability in improving efficiency and reliability. Improving Turbine-L1 to Turbine-L2 or Turbine-L3 does not significantly increase the averaged output of the WEH liquid tank. Compared to the single-rotor case, the MLATS with three rotors can increase the average power output of the WEH liquid tank by up to 40%. However, reliability assessments of Turbine-L3 show that if the side rotor or the middle rotor fails to work, the averaged power output is reduced by 44% and 22%, respectively.

As a future direction, wave-to-wire (W2W) modeling of the present WEH liquid tank should be conducted. Several recent investigations have demonstrated end-to-end W2W modeling frameworks. These frameworks can successfully capture the complete energy conversion process from ocean waves to electricity [3, 51, 52]. There is an emerging trend towards comprehensive system - level modeling and control optimization in the field of wave energy research.

Acknowledgements

This study was funded by National Natural Science Foundation of China (Grant No. 52471271, and U22A20242). The research was partly sponsored by the Shanghai Engineering Research Center of Offshore Wind Energy Development and Utilization Open Project of Shanghai Investigation, Design & Research Institute Co. Ltd (No. FNZX2023KP03-1). This study was also supported by the advanced computing resources provided by the Supercomputing Center of Dalian University of Technology.

Data Availability

The data that support the findings of this study are available from the corresponding author, upon reasonable request.

CRediT authorship contribution statement

Chongwei Zhang: Conceptualisation, Methodology, Data curation, Investigation, Formal analysis, Visualisation, Validation, Software, Resources, Funding acquisition, Supervision, Writing - Original Draft, Writing - Review

Journal Pre-proof

& Editing. **Xunhao Zhu:** Methodology, Data curation, Investigation, Formal analysis, Visualisation, Validation, Software, Writing - Original Draft, Writing - Review & Editing. **Cheng Zhang:** Methodology, Data curation, Investigation, Formal analysis, Visualisation, Validation, Software, Writing - Original Draft, Writing - Review & Editing. **Luofeng Huang:** Methodology, Writing - Review & Editing. **Dezhi Ning:** Methodology, Resources, Funding acquisition, Project administration, Writing - Review & Editing.

Declaration of Generative AI and AI-assisted technologies in the writing process

During the preparation of this work, generative AI and AI-assisted technologies were not used.

References

[1] Clément A, McCullen P, Falcão AFO, Fiorentino A, Gardner F, Hammarlund K, et al. Wave energy in Europe: current status and perspectives. Renew Sust Energ Rev 2002;6(5):405–31.

[2] Liu Z, Xu C, Kim K. Overall performance of a model OWC system under the free-spinning mode: An experimental study. Ocean Eng 2021;227:108890.

[3] Zhang C, Li D, Ding Z, Liu Y, Cao F, Ning D. Wave energy converter with multiple degrees of freedom for sustainable repurposing of decommissioned offshore platforms: An experimental study. Appl Energy 2024;376:124204.

[4] Liu Z, Zhang G. Overtopping performance of a multi-level CROWN wave energy convertor: A numerical study. Energy 2024;294:130795.

[5] Liu Z, Han Z, Shi H, Yang W. Experimental study on multi-level overtopping wave energy convertor under regular wave conditions. Int J Nav Archit Ocean Eng 2018;10(5):651–9.

[6] Vicinanza D, Contestabile P, Quvang Harck Nørgaard J, Lykke Andersen T. Innovative rubble mound breakwaters for overtopping wave energy conversion. Coast Eng 2014;88:154–70.

[7] Zhang C, Dai J, Cui L, Ning D. Experimental study of nonlinear states of oscillating water column in waves. Phys Fluids 2023;35(1):017108.

[8] Mayon R, Ning D, Zhang C, Chen L, Wang R. Wave energy capture by an omnidirectional point sink oscillating water column system. Appl Energy 2021;304:117795.

[9] Carrelhas AAD, Gato LMC, Falcão AFO, Henriques JCC. Control law design for the air-turbine-generator set of a fully submerged 1.5 MW mWave prototype. Part 1: Numerical modelling. Renew Energ 2022;181:1402–18.

[10] Wu B, Li M, Wu R, Zhang Y, Peng W. Experimental study on primary efficiency of a new pentagonal backward bent duct buoy and assessment of prototypes. Renew Energ 2017;113:774–83.

[11] Kim SJ, Koo W, Kim MH. Nonlinear time-domain NWT simulations for two types of a backward bent duct buoy (BBDB) compared with 2D wave-tank experiments. Ocean Eng 2015;108:584–93.

[12] Liu Z, Zhang X, Xu C. Experimental study on a back-bent duct buoy oscillating water column device in various degrees of freedom. Renew Energ 2024;224:120121.

[13] Chen W, Dolguntseva I, Savin A, Zhang Y, Li W, Svensson O, et al. Numerical modelling of a point-absorbing wave energy converter in irregular and extreme waves. Appl Ocean Res 2017;63:90–105.

[14] Lai W, Li D, Xie Y. Numerical study on the improvement design of the oscillating buoy wave energy converter. Ocean Eng 2021;232:109080.

[15] Engström J, Kurupath V, Isberg J, Leijon M. A resonant two body system for a point absorbing wave energy converter with direct-driven linear generator. J Appl Phys 2011;110:124904.

[16] Chen M, Yun Q, Hallak T, Zhou H, Zhang K, Tao T, et al. Comparative Study on the Performances of a Hinged Flap-Type Wave Energy Converter Considering Both Fixed and Floating Bases. J Mar Sci Eng 2024;12:1416.

[17] Renzi E, Abdolali A, Bellotti G, Dias F. Wave-power absorption from a finite array of oscillating wave surge converters. Renew Energ 2013;63:55–68.

[18] Yu H, Zhang Y, Zheng S. Numerical study on the performance of a wave energy converter with three hinged bodies. Renew Energ 2016;99:1276–86.

[19] Wang X, Xia H, Guo Y, Duan Y, Wang M, Liu Y, et al. Research on field testing and assessment technology of ocean energy converters. Ocean Eng 2023;285:115539.

[20] Cordonnier J, Gorintin F, De Cagny A, Clément AH, Babarit A. SEAREV: Case study of the development of a wave energy converter. Renew Energ 2015;80:40–52.

[21] Tiron R, Mallon F, Dias F, Reynaud EG. The challenging life of wave energy devices at sea: A few points to consider. Renew Sust Energ Rev 2015;43:1263–72.

[22] Magnusson AK, Donelan MA. The Andrea Wave Characteristics of a Measured North Sea Rogue Wave. J Offshore Mech Arct Eng 2013;135(3):031108.

[23] McAllister ML, Draycott S, Adcock T, Taylor P, Van Den Bremer T. Laboratory recreation of the Draupner wave and the role of breaking in crossing seas. J Fluid Mech 2019;860:767–86.

[24] Renzi E, Wei Y, Dias F. The Pressure Impulse of Wave Slamming on an Oscillating Wave Energy Converter. J Fluids Struct 2018;82:258.

[25] Medina Rodríguez AA, Posada Vanegas G, Silva Casarín R, Mendoza Baldwin EG, Vega Serratos BE, Puc Cutz FE, et al. Experimental investigation of the hydrodynamic performance of land-fixed nearshore and onshore oscillating water column systems with a thick front wall. Energies 2022;15(7):2364.

[26] Gallutia D, Tahmasbi Fard M, Gutierrez Soto M, He J. Recent advances in wave energy conversion systems: From wave theory to devices and control strategies. Ocean Eng 2022;252:111105.

[27] Wang H, Sun J, Xi Z, Dai S, Xing F, Xu M. Recent Progress on Built-in Wave Energy Converters: A Review. J Mar Sci Eng 2024;12(7):1176.

Journal Pre-proof

[28] Viet NV, Xie X, Liew KM, Banthia N, Wang Q. Energy harvesting from ocean waves by a floating energy harvester. Energy 2016;112:1219–26.
[29] Viet NV, Wang Q. Ocean wave energy pitching harvester with a frequency tuning capability. Energy 2018;162:603–17.
[30] Clemente D, Rosa-Santos P, Taveira-Pinto F, Martins P, Paulo-Moreira A. Proof-of-concept study on a wave energy converter based on the roll oscillations of multipurpose offshore floating platforms. Energy Convers Manag 2020;224:113363.
[31] Jin C, Kang H, Kim M, Bakti FP. Performance evaluation of surface riding wave energy converter with linear electric generator. Ocean Eng 2020;218:108141.
[32] Pozzi N, Bracco G, Passione B, Sirigu SA, Mattiazzo G. PeWEC: Experimental validation of wave to PTO numerical model. Ocean Eng 2018;167:114–29.
[33] Jiang X, Shi H, Cao F, Zhao Z, Li M, Chen Z. System analysis and experimental investigation of a pendulum-based wave energy converter. Ocean Eng 2023;277:114300.
[34] Townsend NC, Shenoi RA. Modelling and analysis of a single gimbal gyroscopic energy harvester. Nonlinear Dyn 2013;72:285–300.
[35] Vissio G, Valério D, Bracco G, Beirão P, Pozzi N, Mattiazzo G. ISWEC linear quadratic regulator oscillating control. Renew Energ 2017;103:372–82.
[36] Zhang C, Ding Z, Chen L, Ning D. Sloshing dynamics of liquid tank with built-in buoys for wave energy harvesting. J Fluids Struct 2022;113:103662.
[37] Gunawardane SDGSP, Bandara GACT, Lee YH. Hydrodynamic analysis of a novel wave energy converter: Hull Reservoir Wave Energy Converter (HRWEC). Renew Energ 2021;170:1020–39.
[38] Kim BH, Wata J, Zullah MA, Ahmed MR, Lee YH. Numerical and experimental studies on the PTO system of a novel floating wave energy converter. Renew Energ 2015;79:111–21.
[39] Ding H, Zhou T, Wang J, Altay O, Zhang J. Energy harvesting in tuned liquid column dampers using Savonius type hydrokinetic turbines. Mech Syst Signal Process 2023;186:109846.
[40] Ribeiro e Silva S, Gomes RPF, Lopes BS, Carrelhas A, Gato LMC, Henriques JCC, et al. Model testing of a floating wave energy converter with an internal U-shaped oscillating water column. Energy Convers Manag 2021;240:114211.
[41] Fonseca N, Pessoa J, Ribeiro e Silva S, Le Boulluec M, Ohana J. Model tests of a wave energy converter based on water oscillating in a U tank. Nantes, France: In: Proceeding of 12me JournTes de l'hyrodynamique; 2010, p. 17–9.
[42] Fonseca N, Pessoa J. Numerical modeling of a wave energy converter based on U-shaped interior oscillating water column. Appl Ocean Res 2013;40:60–73.
[43] Ribeiro e Silva S, Gomes RPF, Falcao AFO. Hydrodynamic optimization of the UGEN: Wave energy converter with U-shaped interior oscillating water column. Int J Mar Energy 2016;15:112–26.
[44] Thakker A, Dhanasekaran TS. Computed effects of tip clearance on performance of impulse turbine for wave energy conversion. Renew Energ 2004;29:529–47.
[45] Ciappi L, Stebel M, Smolka J, Cappietti L, Manfrida G. Analytical and computational fluid dynamics models of wells turbines for oscillating water column systems. J Energy Resour Technol 2021;144(5):050903.
[46] Falcão AF, Henriques JC, Gomes RP, Portillo JC. Theoretically based correction to model test results of owc wave energy converters to account for air compressibility effect. Renew Energ 2022;198:41–50.
[47] Falcão AF, Henriques JC. The spring-like air compressibility effect in oscillating-water-column wave energy converters: Review and analyses. Renew Sust Energ Rev 2019;112:483–98.
[48] Song SK, Park JB. Control Strategy of an Impulse Turbine for an Oscillating Water Column-Wave Energy Converter in Time-Domain Using Lyapunov Stability Method. Appl Sci 2016;6(10):281.
[49] Kuczmann M. Review of dc motor modeling and linear control: Theory with laboratory tests. Electronics 2024;13(11):2225.
[50] Zhang C, Zhu X, Zhang C, Huang L, Ning D. Coupled hydro-aero-turbo dynamics of liquid-tank system for wave energy harvesting: Numerical modellings and scaled prototype tests. 2025. URL: https://arxiv.org/abs/2502.10800. arXiv:2502.10800.
[51] Henriques J, Portillo J, Sheng W, Gato L, Falcão AFO. Dynamics and control of air turbines in oscillating-water-column wave energy converters: Analyses and case study. Renew Sust Energ Rev 2019;112:571–89.
[52] Ciappi L, Simonetti I, Bianchini A, Cappietti L, Manfrida G. Application of integrated wave-to-wire modelling for the preliminary design of oscillating water column systems for installations in moderate wave climates. Renew Energ 2022;194:232–48.

Journal Pre-proof

Highlights:

- Multi-layered air turbine is considered for wave-energy-harvesting liquid tank.
- Integrated numerical model is developed to study coupled hydro-aero-turbo dynamics.
- Scaled prototype is manufactured and tested for numerical validation.
- Inherent mechanisms of liquid tank system are systematically investigated.

Journal Pre-proof

Journal Pre-proof

Declaration of interests

☒ The authors declare that they have no known competing financial interests or personal relationships that could have appeared to influence the work reported in this paper.

☐ The authors declare the following financial interests/personal relationships which may be considered as potential competing interests:

Journal Pre-proof



https://dspace.org/

Coupled hydro-aero-turbo dynamics of liquid-tank system for wave energy harvesting: numerical modellings and scaled prototype tests

Zhang, Chongwei; Zhu, Xunhao; Zhang, Cheng; Huang, Luofeng; Ning, Dezhi

2025-09
Elsevier
https://doi.org/10.1016/j.energy.2025.136690
Zhang C, Zhu X, Zhang C, et al., (2025) Coupled hydro-aero-turbo dynamics of liquid-tank system for wave energy harvesting: numerical modellings and scaled prototype tests. Energy, Volume 330, September 2025, Article number 136690

Downloaded from a DSpace repository. https://dspace.org/